Natural carbon release compensates for anthropogenic carbon uptake when Southern Hemispheric westerlies strengthen

L. Menviel [1,2,3], D. Waugh [1,3,4], P. Spence [3,5], M. A. Chamberlain [6], V. Lago[1], Z. Li[1], M.H. England[1,3]

[1]Climate Change Research Centre, University of New South Wales, Sydney, Australia
[2]Earth and Sustainability Science Research Centre, University of New South Wales, Sydney, Australia
[3]The Australian Centre for Excellence in Antarctic Science, University of Tasmania, Hobart, Tasmania 7001, Australia
[4]Dpt. of Earth and Planetary Sciences, John Hopkins University, Baltimore, USA
[5]Institute for Marine and Antarctic Studies, University of Tasmania, Hobart, Australia
[6]CSIRO Oceans and Atmosphere, Hobart, Australia

Key Points:

- Sensitivity experiments suggest that as SH westerlies increase and shift poleward, contemporary CO_2 uptake in the SO decreases.
- An eddy-permitting simulation suggests that the SO CO_2 uptake has stagnated between 1980 and 2007 due to stronger SH westerlies.
- The simulation exhibits decadal-scale variability with a minimum in SO natural CO_2 uptake in 2000 due to strong westerlies.

Corresponding author: L. Menviel, l.menviel@unsw.edu.au

Abstract

The Southern Ocean (SO) provides the largest oceanic sink of carbon. Observational datasets highlight decadal-scale changes in SO CO_2 uptake, but the processes leading to this decadal-scale variability remain debated. Here, using an eddy-permitting ocean, sea-ice, carbon cycle model, we explore the impact of changes in Southern Hemisphere (SH) westerlies on contemporary (i.e. total), anthropogenic and natural CO_2 fluxes using idealised sensitivity experiments as well as an interannually varying forced (IAF) experiment covering the years 1948 to 2007. We find that a strengthening of the SH westerlies reduces the contemporary CO_2 uptake by leading to a high southern latitude natural CO_2 outgassing. The enhanced SO upwelling and associated increase in Antarctic Bottom Water decrease the carbon content at depth in the SO, and increase the transport of carbon-rich waters to the surface. A poleward shift of the westerlies particularly enhances the CO_2 outgassing south of 60°S, while inducing an asymmetrical DIC response between high and mid southern latitudes. Changes in the SH westerlies in the 20th century in the IAF experiment lead to decadal-scale variability in both natural and contemporary CO_2 fluxes. The ∼10% strengthening of the SH westerlies since the 1980s led to a 0.016 GtC/yr^2 decrease in natural CO_2 uptake, while the anthropogenic CO_2 uptake increased at a similar rate, thus leading to a stagnation of the total SO CO_2 uptake. The projected poleward strengthening of the SH westerlies over the coming century will thus reduce the capability of the SO to mitigate the increase in atmospheric CO_2.

Plain Language Summary

The Southern Ocean (SO) is the largest oceanic sink of anthropogenic carbon. The Southern Hemispheric (SH) westerlies significantly impact SO dynamics and atmospheric CO_2 uptake. While a strengthening of SH westerlies enhances the uptake of anthropogenic CO_2 it leads to enhanced outgassing of natural CO_2, thus reducing the total CO_2 uptake. The current and projected poleward strengthening of the SH westerlies over the coming century reduces the capability of the SO to mitigate the increase in atmospheric CO_2 concentration.

1 Introduction

As a result of anthropogenic emissions, atmospheric CO_2 concentration (CO_{2atm}) has increased from a natural level of 277 ppm in 1750 (Joos & Spahni, 2008) to 405 ppm in 2017 (Le Quéré et al., 2018). Over the period 1870-2017, the total emissions of anthropogenic carbon are estimated at 615 GtC, but this is associated with a net uptake of 190 GtC by the terrestrial biosphere, and 150 GtC by the ocean (Le Quéré et al., 2018). The terrestrial biosphere and the ocean have thus strongly mitigated the anthropogenic emissions of carbon, respectively absorbing ∼31% and 24% of the emissions.

The largest oceanic carbon sink is the Southern Ocean (SO), which has contributed ∼40% of the global oceanic CO_2 uptake in the 1990s (Sabine et al., 2004; Mikaloff-Fletcher et al., 2006). The oceanic CO_2 uptake is, however, spatially and seasonally variable. Winter mixing leads to an increase in the concentration of DIC at the surface, thus increasing surface ocean pCO_2, while biological productivity draws down DIC in summer. In the Antarctic Southern Zone and polar frontal zone, there is a maximum CO_2 uptake in austral summer and a minimum uptake or even outgassing in austral winter (Gray et al., 2018). On the other hand, there is an oceanic CO_2 uptake year round in the subtropical zone of the SO, peaking in austral winter.

There is evidence for large decadal variability in the SO carbon uptake (Li & Ilyina, 2018). Observational estimates, covering the period 1982-2011, suggest the total carbon uptake in SO was slower than expected in the 1990s, but has increased significantly since 2002 to reach a maximum of 1.2 PgC. yr^{-1} in 2011 (LeQuéré et al., 2007; Land-

schützer et al., 2015; Gruber, Landschützer, & Lovenduski, 2019). There is, however, significant uncertainty associated with these estimates due to the sparsity of the data, particularly in the 1990s (Ritter et al., 2017), and little information prior to 1982. It has furthermore been suggested that this data scarcity might lead to a 39% overestimation of the the amplitude of SO decadal CO_2 uptake variability (Gloege et al., 2021).

The weaker SO carbon uptake observed in the 1990s has been attributed to a positive trend in the Southern Annular Mode (SAM) (Marshall, 2003; LeQuéré et al., 2007; Lenton & Matear, 2007; Lovenduski et al., 2007, 2008). The SO circulation is mostly driven by SH westerly winds, which generate an equatorward Ekman transport and an associated upwelling of carbon-rich deep waters. Changes in the position and strength of the SH westerlies are linked to the dominant mode of atmospheric variability in the southern hemisphere, the SAM. Positive SAM trends, which are associated with poleward contraction and stronger than average westerly winds, have been observed since 1979, particularly during austral summer and autumn (Fogt & Marshall, 2020).

Numerical studies have highlighted the role of SH westerlies in modulating the upwelling of DIC rich deep water and thus the exchange between atmospheric and oceanic carbon. Stronger SH westerlies enhance the SO upwelling, leading to an oceanic loss of carbon and thus an increase in CO_{2atm} (Toggweiler, 1999; Lauderdale et al., 2013; Munday et al., 2014; Lauderdale et al., 2017; Menviel et al., 2018). The outgassing of natural carbon as a result of stronger SO upwelling could however be partly mitigated by enhanced export production at the surface of the SO (Menviel et al., 2008; Hauck et al., 2013). In addition, the impact of latitudinal changes in the position of the SH westerlies on oceanic carbon and CO_{2atm} is less robust, as it might depend on the initial position of the SH westerlies and on how the latitudinal change in the SH westerly impact the oceanic circulation (Völker & Köhler, 2013; Lauderdale et al., 2013, 2017).

Most of the numerical studies analysing the impact of SH westerly changes mentioned above focused on natural carbon, but given the increase in anthropogenic carbon emissions since 1870, the natural carbon cycle has been perturbed, and the impact of changes in the strength and position of the SH westerly winds on anthropogenic and total carbon uptake also needs to be taken into account. A few studies performed with coarse resolution ocean models (Lenton & Matear, 2007; Lovenduski et al., 2007, 2008) showed that positive phases of the SAM lead to an outgassing of natural CO_2, while enhancing the uptake of anthropogenic CO_2, thus leading to a reduction in the total CO_2 uptake.

While changes in the SAM seem to be the prevailing hypothesis to explain a lower than expected total CO_2 uptake in the 1990s, it was found that changes in heat and freshwater fluxes reduce the impact of these stronger winds (Matear & Lenton, 2008). Landschützer et al. (2015) also suggested that the re-invigoration of the carbon uptake in the SO could not be attributed to the SAM because the ERA-interim reanalysis did not display the associated wind changes, and instead attributed the enhanced carbon uptake to increased solubility in the Pacific sector of the SO due to surface cooling, and a weaker upwelling of DIC-rich waters in the Atlantic and Indian sectors of the SO. McKinley et al. (2020) went one step further and instead suggested that the lower 1990s CO_2 uptake was instead a response to the slower CO_{2atm} growth rate.

There is thus not only uncertainties in the decadal variability but also the processes controlling SO carbon uptake, and there is a need for further studies examining these issues. In addition, there is a need to include the impacts of mesoscale eddy activity. The prevalent mesoscale eddy activity in the SO significantly influences the heat and salt transport and thus SO circulation. Mesoscale eddies drive a southward transport opposing the Ekman northward transport in the SO, and the response of the ocean circulation to changes in the winds can vary substantial due to these eddies. For example, a doubling of the magnitude of SH westerly winds doubles the simulated circumpolar transport in coarse resolution models that do not resolve eddies, but this doubling does not occur in

eddy-resolving simulations (Munday et al., 01 Mar. 2013). Further, (Dufour et al., 2013) has shown that even though a strengthening and poleward shift of the SH westerlies, representing positive phases of the SAM, leads to stronger Ekman-induced northward natural DIC transport, a third of this is compensated by enhanced southward natural DIC transport through eddies.

Here, we perform a suite of simulations with an eddy-permitting ocean, sea ice, biogeochemical model to fill in the above gaps. Specifically we perform (i) simulations with changes in the strength and latitudinal position of SH westerly winds to quantify the impact of these changes on the natural, anthropogenic and total carbon budget, and (ii) a simulation with inter annually varying forcing (IAF) over the period 1948-2007 to examine the decadal variability in SO carbon fluxes and uptake. The model and simulations are described in the next section, and results for the idealized simulation and inter annual forced simulations presented in Sections 3.1 and 3.2 respectively. Discussion and conclusions are in the final paragraph.

2 Methods

Changes in SO carbon uptake are examined using simulations performed with a mesoscale eddy-permitting global ocean, sea-ice, Nutrient-Phytoplankton-Zooplankton-Detritus (NPZD) model (Menviel et al., 2018). The ocean-sea ice model is the MOM5 ocean model (Griffies, 2012) coupled to the dynamic/thermodynamic Sea Ice Simulator (SIS), configured with 1/4° Mercator horizontal resolution, and 50 vertical levels (Spence et al., 2017). This model is coupled to the WOMBAT (Whole Ocean Model with Biogeochemistry and Trophic-dynamic) NPZD model (Kidston et al., 2011; Oke et al., 2013; Law et al., 2017). The physical and biogeochemical parameters are tuned to reduce bias in the ocean state compared to observations, and to reduce the drift in biogeochemical fluxes. The ocean model uses Redi diffusivity (600 m^2/s) and Gent McWilliams (GM) skew diffusion (600 m^2/s) parameterizations to compensate for unresolved mesoscale processes and to improve the simulated Antarctic Bottom Water (AABW) transport and the 3-D distribution of ocean biogeochemical tracers relative to observations. For instance, dissolved oxygen in SO and alkalinity of bottom waters penetrating into ocean basins. This eddy-permitting ocean model allows us to better represent many key features of the ocean circulation (e.g. boundary currents, bathymetry, and eddies). However, we cannot effectively evaluate the importance of eddy compensation in changes of the MOC (or eddy saturation of the ACC), because the model still requires parameterizations (e.g. GM diffusion) to account for the unresolved eddy effects. While the GM component effectively compensates for the advective MOC transport at steady state, the GM transport does not respond the same as resolved eddies to changes forcing and are unable to appropriately represent eddy compensation and saturation (Hofmann & Maqueda, 2011; Farneti et al., 2015; Sinha & Abernathy, 2016).

WOMBAT includes DIC, alkalinity, oxygen, phosphate and iron, that are linked to the phosphate uptake and remineralisation through a constant Redfield ratio. The biogeochemical parameters are based on those of the ACCESS-ESM1.5 (Ziehn et al., 2020), with modifications of the detritus sinking rate (20 m/day), the background iron concentration (0.3 μmol Fe/m^3) and the inorganic production fraction (0.0653), which improve the biogeochemical simulation in the 1/4° ocean model. The air-sea CO_2 exchange is a function of wind speed (Wanninkhof, 1992) and sea ice concentration. Two DIC tracers are included, a natural DIC and a total DIC, with the difference between the two providing an estimate of anthropogenic DIC. The natural DIC exchanges carbon with a constant pre-industrial atmospheric CO_2 concentration of 284 ppm, whereas the total DIC exchanges carbon with the time evolving, observed pCO_2, which takes into account the current increase due to anthropogenic emissions. For the total DIC tracer the atmospheric CO_2 concentration increases from 310 ppm at year 1948 to 391.6 ppm at year 2011, with an average rate of increase of 1.6 ppm/yr (Fig. 7a). Note, physical and biogeochemical

changes in the ocean simulations do not impact the atmospheric state, and in all simulations pCO_2 for the radiative forcing is the same.

To examine the impact of changes in SH winds on natural and anthropogenic carbon, a suite of simulations is performed (Table 1). The model is initialised with modern-day temperature and salinity distributions, and biophysical fields derived from an observation-based climatology (Olsen et al., 2016). The model is first spun-up for 700 years with version 2 of the Coordinated Ocean-ice Reference Experiments (CORE) Normal Year Forcing (NYF) reanalysis data (Griffies et al., 2009), which provides a climatological mean atmospheric state for equilibrating ocean models at 6-hour intervals for 1 year, including synoptic variability. The model uses bulk formulae for air-sea fluxes as described in Griffies et al. (2009). During the 700 years spin up only the natural DIC tracer is active. After this equilibration, the model is run from year 1840 to 2011 with the NYF, and with the total DIC tracer being forced by observed atmospheric CO_2 concentration, to obtain the *control* simulation. The drift in *control* is reasonable, with a DIC drift of -0.0123 mmol/m^3 in the SO, and -0.0194 mmol/m^3 in the deep ocean south of 20°S. There is no significant drift in the air-sea CO_2 flux.

Three idealised wind perturbation experiments, in which the SH near surface wind speeds are abruptly modified, are initiated from atmospheric CO_2 year 1970 of the NYF *control* simulation (Table 1). The wind perturbations are applied in the same manner as described in (Hogg et al., 2017). The zonally uniform and temporally steady perturbations are applied to the CORE-NYF 6-hourly wind field between 25°S and 70°S with smoothing within 5° latitude of the perturbation boundaries. Changes in the surface wind speed impact the windstress, as well as the buoyancy fluxes between the atmosphere and ocean. In the *strong* simulation the zonal and meridional components of the windstress are increased by ∼20% between 32°S and 65°S, whereas they are decreased by ∼16% in *weak* (Fig. 2). In the *strong/shift* perturbation, the strong forcing is combined with a ∼4°S shift of the SH winds between 32°S and 65°S. The magnitude of the changes in these perturbation simulations is based on late 21^{st} century projections from CMIP5 models (Zheng et al., 2013), and the methodology follows Hogg et al. (2017). All perturbation simulations are integrated for 42 years, with the pCO_2 representing years 1970 to 2011.

The model setup and wind perturbation experimental design are similar to the one employed in a series of previous ocean circulation studies (Spence et al., 2014; Hogg et al., 2017; Downes et al., 2017; Waugh et al., 2019), except that the previous simulations did not use neutral ocean physics parameterisations. In the simulations presented here, as well as the one described in Menviel et al. (2018), neutral physics parameterisations are used to improve the representation of ocean tracers relative to observations. A brief overview of the natural carbon cycle response to the *strong/shift* experiment is presented in Menviel et al. (2018), and a comparison of the simulated *control* biogeochemical fields against observations is shown in the supplementary material of Menviel et al. (2018).

To better constrained the impact of varying westerlies on the oceanic carbon uptake over the 2nd half of the 20th century, a more realistic simulation is performed, forced with the time-evolving atmospheric forcing derived from the CORE IAF version 2 (Large & Yeager, 2009) from 1948 to 2007. CORE-IAF provides air-sea fluxes of momentum, heat and freshwater at time intervals ranging from 6 hours to one month. This simulation is referred to as the *IAF* simulation. The *IAF* simulation is initialised from the NYF control simulation at year 1948. Comparison of the *IAF* and *control* simulations aims to show the impact of time-varying atmospheric forcing on the oceanic carbon cycle. In previous studies we found that the SH wind trend dominates the modelled Southern Ocean response to the IAF forcing by isolated the historical trends in surface heat, freshwater and momentum fluxes. Certainly, in the future the influence of increasing surface heating and freshwater fluxes (including glacial melt water trends which are not part of the IAF forcing) on the Southern Ocean will increase.

To better understand the drivers of changes in ocean-atmosphere CO_2 fluxes, changes in natural surface water pCO_2 are decomposed into their natural DIC, alkalinity (ALK) and solubility (sea surface salinity, SSS and sea surface temperature, SST) contributions in the following way (Sarmiento & Gruber, 2006):

$$\Delta pCO_2 = \Delta pCO_{2DIC} + \Delta pCO_{2ALK} + \Delta pCO_{2SST} + \Delta pCO_{2SSS} \quad (1)$$

For DIC, ALK and SSS, ΔpCO_2 is:

$$\Delta pCO_{2X} = \Delta X * \gamma_X * \overline{p}CO_2 / \overline{X} \quad (2)$$

where $\overline{X}$ represents the surface pCO_2, and mean DIC, ALK or SSS value in *control*. γ_{DIC} is the high-latitude Revelle factor and is equal to 13.3. γ_{ALK} is the high-latitude sensitivity factor equal to -12.6 and γ_{SSS} is equal to 1.

The SST contribution is derived from

$$\Delta pCO_{2SST} = e^{(\Delta SST * \gamma_{SST})} * \overline{p}CO_2 - \overline{p}CO_2 \quad (3)$$

where γ_{SST} is equal to $0.0423/°$.

3 Results

3.1 Idealized experiments

3.1.1 Changes in SO CO_2 fluxes as a response to varying SH westerlies

The SO tracers, mixed layer depth and circulation features in the NYF *control* simulation are in good agreement with observations. For example, the transport through Drake Passage is 135 Sv (Fig. S1) and the lower cell of the overturning circulation (shown in blue at density $\geq$1036.8 kg/m^3, referenced at 2000m depth) is relatively well represented with a transport of 25.5 Sv in *control* (Fig. 1a). The values, as well as horizontal and vertical ocean gradients of the simulated biogeochemical fields in *control* are in overall agreement with observations (Menviel et al., 2018). The DIC and alkalinity values in the intermediate North Atlantic and SO are however slightly underestimated, while they are overestimated in the intermediate North Pacific.

In the *control* NYF run at years 2007-2011, the SO is a net sink of contemporary (i.e. total) carbon (Fig. 2f, black), taking up 1.73 GtC/yr south of 35°S and with the maximum uptake occurring between 35°S and 50°S. Due to the upwelling of DIC-rich deep waters occurring south of ~55°S, the contemporary carbon uptake is small there. In fact, if the atmospheric CO_2 concentration was at pre-industrial levels (i.e. 284 ppm), there would be an outgassing of natural CO_2 south of ~55°S, in the order of 0.24 GtC/yr (Figs. 2d, 3b). Through Ekman transport, mixed layer waters in SO move equatorward, and nutrients and DIC are consumed by phytoplankton, leading to a natural CO_2 uptake between 52°S and 35°S, latitudes at which the Antarctic Intermediate Waters (AAIW) and the sub-Antarctic mode waters (SAMW) are formed.

Changes in the strength and location of the SH westerlies (Table 1) impact both the natural and anthropogenic air-sea CO_2 fluxes (Fig. 2). The stronger upwelling in experiment *strong* leads to a higher outgassing of natural carbon south of 49°S (from 0.21 GtC/yr in *control* to 0.77 GtC/yr in *strong*), and reduces the uptake of natural carbon between 42°S and 49°S (from -0.36 to -0.18 GtC/yr, Figs. 2d and 3e,f). While the uptake of anthropogenic carbon is also higher south of 50°S, the resultant contemporary carbon uptake over the SO is reduced by 21% in *strong* compared to *control* as the changes in natural CO_2 flux dominates.

The reverse is simulated when the westerlies are weaker, with enhanced natural carbon uptake but reduced anthropogenic carbon uptake, leading to a 9% increase in contemporary carbon uptake over the SO in *weak* compared to *control* (Figs. 2 and 3c,d).

If the winds are also shifted poleward (*strong/shift*), there is both a stronger outgassing of natural carbon and enhanced anthropogenic carbon uptake south of 50°S compared to *control*. If compared to the *strong* experiment, then there is a stronger outgassing of natural CO_2 south of 57°S, however, the ougassing is slightly reduced between 48°S and 58°S and the uptake stronger between 40°S and 48°S. As a result, the overall impact on the contemporary carbon uptake is similar to *strong* with a 21% lower contemporary carbon uptake over the SO compared to *control*.

The results of the above analysis are summarised in Fig. 4, which shows a close to linear relation for each CO_2 flux with windstress magnitude. As the windstress increases over the SO, the contemporary CO_2 uptake decreases by 6 GtC/yr per N/m^2. As the windstress increases the natural CO_2 outgassing south of 50°S and the SO switches from being a net sink to a net source of natural CO_2 (11.8 GtC/yr per N/m^2). This is partly compensated by enhanced anthropogenic CO_2 uptake with windstress (-6.2 GtC/yr per N/m^2).

3.1.2 Attribution of surface pCO_2 changes

To understand the changes in CO_2 fluxes resulting from the varying SO windstress, an attribution of surface pCO_2 changes to natural DIC, ALK, SST and SSS is performed on the idealised experiments (Fig. 3i-k). This analysis shows that the changes in natural DIC and ALK drive the changes in natural CO_2 flux. As the SO upwelling strengthens in *strong*, it increases the DIC and ALK concentration at the surface of the SO. A greater DIC concentration increases surface pCO_2 by about 24 ppm between 45°S and 60°S, however greater ALK decreases pCO_2 by about 12 ppm in the same region (Fig. 3j). The reverse is simulated when the SO upwelling is reduced in *weak*, with a surface pCO_2 decrease due to the lower DIC, and a slight pCO_2 increase due to the associated lower ALK (Fig. 3i). While changes in surface salinity are negligible, due to surface fluxes being kept constant, SST changes provide a small negative feedback. There is a small global cooling (-0.4°C) at the surface of the SO in experiment *strong*, with up to -2°C locally in the meanders off New Zealand and South Africa, thus leading to a ∼3.5 ppm lower surface pCO_2 between 35°S and 55°S. The reverse is observed in experiment *weak* with a 0.3°C SO warming, with up to 1.8°C locally (Fig. 3i). These temperature changes are mostly due to the influence of the winds on SO isopycnals. Stronger westerlies lead to a steepening of the isopycnals, and thus a slight equatorward shift of the front.

Similarly to *strong*, the *strong/shift* experiment displays relatively large (∼20-24 ppm) positive surface pCO_2 anomalies mostly due to increased DIC (Fig. 3k). These anomalies are however displaced ∼5° poleward compared to *strong*. This poleward shift also leads to larger surface ALK anomalies, thus providing a stronger compensating effect. However, the largest surface pCO_2 anomalies are due to DIC increase near the Antarctic coast resulting from enhanced deep-ocean convection. This is associated with a surface ocean warming, which provides a small positive contribution (2 ppm) to the surface pCO_2 increase (Fig. 3k).

The changes in minimum and maximum sea-ice cover between experiments *strong*, *weak* and *control* are very small, and therefore do not contribute significantly to the observed changes in CO_2 flux (Fig. 3). However, the poleward shifted westerlies in experiment *strong/shift* lead to the opening of a polynya between 60°S and 70°S in the Weddell Sea (not shown here) (Hogg et al., 2017; Menviel et al., 2018). This polynya induces a strong deep-ocean convection event in late winter/spring, which leads to a natural CO_2 outgassing.

3.1.3 Changes in oceanic DIC

As discussed above, the outgassing of natural carbon in the SO increases with windstress as the upwelling of DIC-rich waters is enhanced (Fig. 4). A strengthening of the SH westerlies enhances both the lower and upper overturning cells, with stronger AAIW and AABW transport by up to 8 and 10 Sv, respectively in *strong* compared to *control* (Fig. 1). The natural DIC concentration within AABW (σ >1027.75 kg/m^3) is thus lower in *strong* (-2.24 mmol/m^3) and higher in *weak* (+0.58 mmol/m^3) compared to *control* (Figs. 5a-c and 6a, black). A lower natural DIC concentration with a strengthening of the SH westerlies is also seen within AAIW (1027.4 > σ >1027 kg/m^3), with a 4.7 mmol/m^3 decrease in *strong*, and 4.0 mmol/m^3 increase in *weak*.

The strong ventilation of abyssal and deep waters in *strong/shift* lowers the natural DIC concentration by 8.5 mmol/m^3 within AABW. On the other hand, the DIC concentration increases north of 40°S in the upper 2000 m compared to *strong* (Fig. 5c). Within SAMW (1027 > σ >1026.7 kg/m^3), the natural DIC increases in *strong/shift* by 7.5 mmol/m^3, whereas it decreases by 0.6 mmol/m^3 in *strong* (Figs. 5c and 6c). This DIC increase is also consistent with an increase in the age of the watermass, previously identified in Waugh et al. (2019), which could be due to a decrease in SAMW subduction (Downes et al., 2017).

These natural DIC changes can be decomposed into their organic, carbonate and preformed components (Text S1) to better assess the processes involved. The SH westerly strengthening in *strong* leads to a ∼10 mmol/m^3 decrease in regenerated DIC everywhere in SO (Fig. S2), which is partly compensated by an increase in preformed DIC. The carbonate component leads to positive anomalies in the upper 1000m, and particularly between 40°S and 60°S. This is a result of the 8 to 9% increase in primary and export production in SO and associated enhanced carbonate dissolution at intermediate depth of the SO. A similar picture emerges in *strong/shift*, but with an amplitude twice as large. This weaker biological pump efficiency in *strong* and *strong/shift* results from the lower residence time of the waters in the SO, which is primarily a function of the stronger AABW formation and transport and SO upwelling rate.

The strength of the winds also impacts the distribution of anthropogenic DIC with the pattern of change being similar to that of natural DIC except of opposite sign. A windstress increase results in higher anthropogenic DIC concentration everywhere in the SO (Figs. 5e and 6 blue). Specifically, the anthropogenic DIC concentration (for years 2007-2011) in *strong* is 0.93 mmol/m^3, 1.25 mmol/m^3 and 0.7 mmol/m^3 higher in AABW, AAIW and SAMW, respectively than in *control*. Similarly, the anthropogenic DIC concentration is lower in *weak* than in *control* with a large change (∼1.9 mmol/m^3) in AAIW and SAMW, but only a slight decrease within AABW.

The anthropogenic DIC concentration in AABW, AAIW, and SAMW is much higher in *strong/shift* than *control*, with increases of 2.71 mmol/m^3, 2.05 mmol/m^3, and 3.2 mmol/m^3, respectively (Figs. 5f and 6, blue star). This larger anthropogenic carbon uptake is related to the polynya opening and associated strengthened deep-ocean convection in *strong/shift*.

Overall, natural DIC changes dominate the total DIC concentration change within all watermasses and in all experiments (Fig. 5g-i), with a decrease in total DIC as the wind increases within AABW and AAIW (Fig. 6a,b). The changes within SAMW are much smaller, and are dominated by the *strong/shift* experiment, which records an increase in natural and total DIC concentration due to the poleward shift of the winds. The changes in natural DIC dominate the changes in total DIC because the vertical advection of carbon into the mixed layer through Ekman divergence in the SO dominates the carbon budget (Fig. S3). Vertical DIC advection into the upper 200m due to Ekman divergence south of 50°S is also about twice as large as subduction north of 50°S in *strong*, with the reverse being true for *weak*. Changes in primary production, which

provide an upper estimate of changes in export production, provide a negative feedback north of 50°S, but are two order of magnitude lower than changes in vertical advection (Fig. S3), in agreement with previous studies (Hauck et al., 2013).

3.2 IAF experiment

3.2.1 SO CO_2 fluxes

We now consider the changes in air-sea CO_2 fluxes in the *IAF* simulation, in which the SH westerlies increase from ∼0.09 N/m^2 in 1948-1952 to ∼0.13 N/m^2 in 2003-2007 (Fig. 7b, Table 1). While the westerlies also shift poleward by ∼3.5° in that experiment, the poleward shift occurs between 1948 and 1974 (Fig. 7c). After that, the mean latitudinal position of the maximum SO windstress stays relatively constant at ∼52°S. *IAF* simulates strong decadal-scale variability in natural CO_2 and thus contemporary CO_2 uptake (orange curve in Fig 7g). A 0.01 GtC/yr^2 increase in contemporary CO_2 uptake between 1948 and 1975 is also simulated. However, the uptake stays relatively constant between 1980 and 2007, at a mean value of 1.36 GtC/yr. While the *IAF* and *control* display similar trends between 1970 and 1980, the contemporary CO_2 uptake in *control* keeps on increasing linearly between 1992 and 2007 (black line in Fig 7g) in contrast to *IAF*.

The simulated contemporary CO_2 fluxes in *IAF* can be compared to observational estimates derived from the self-organizing map-feed-forward neural network (SOM-FFN) dataset (Landschützer et al., 2016). As the SOM-FFN is available for the period 1982-2015, we compare simulation and observational estimate for the overlapping period of 1982-2007 (grey line in Fig 7g). There is poor agreement in between the variations in contemporary air-sea CO_2 fluxes in *IAF* and the fluxes inferred from SOM-FFN (Landschützer et al., 2016) between 1982 and 1990, however the *IAF* simulation and observations are in close agreement between 1991 and 2007 (Fig. 1e, R=0.41 between 1982 and 2007 and R=0.72 between 1991 and 2007). Both simulation and observations suggest a maximum oceanic CO_2 uptake in the early 1990s and late 2000s, and a minimum uptake between 1998 and 2001. This reduced uptake between 1998 and 2001 is however under-estimated in our simulation. In addition, the mean simulated CO_2 uptake is overestimated by ∼0.5 GtC/yr.

This contemporary CO_2 flux can be decomposed into anthropogenic and natural contributions. The SO anthropogenic CO_2 uptake increases from 0.6 to 1.2 GtC/yr (Fig 7f), and becomes larger than *control* after 1992. However, the uptake of natural CO_2 south of 35°S decreases from 0.68 to 0.24 GtC/yr between 1970 and 2007. Since the early 1980s the simulated natural CO_2 uptake decreases at a rate of 0.016 GtC/yr^2. The stagnation of the contemporary CO_2 uptake since ∼1980 is thus likely due to changes in the atmospheric forcing, and in particular the increase in the SH westerlies. The strength of the SH westerlies varies significantly on an interannual and decadal timescale in *IAF*, but both the natural and contemporary CO_2 fluxes are well correlated to the wind changes (Fig. 7), with stronger SH winds linked to reduced uptake of natural CO_2 (R=-0.83). As in the idealised experiments, stronger and poleward shifted westerlies strengthen AABW formation and transport (Fig. 7d). Changes in natural carbon uptake are strongly correlated to changes in AABW (R=-0.91), with stronger AABW linked to higher natural CO_2 outgassing south of 50°S . The maximum mixed layer depth in the Weddell Sea is deeper over years 2003-2007 than 1948-1952 (Fig. S4), consistent with the stronger AABW transport.

The pattern of simulated and observed surface contemporary pCO_2 trends in the 1990s (taken here are 1992 to 2001) and the 2000s (taken here as 2001 to 2006) are shown in Figure 8. Both simulation and observation display a ∼50% larger contemporary pCO_2 trend in the 1990s than 2000s north of 60°S, while the CO_{2atm} rate of increase was 1.6 ppm/yr in 1990s compared to 2.1 in 2000s, indicating a re-invigoration of the SO CO_2 sink.

In agreement with observations, the *IAF* simulates the maximum pCO_2 trend in the South Pacific in the 1990s (Fig. 8a,e). A maximum trend in the Pacific between 60°S and 50°S is also seen in the simulated natural pCO_2 trend (Fig. 8g). The decomposition into the non-thermal (DIC+ALK) and thermal trends shows that this is due to the non-thermal trend, with an increase in contemporary DIC, principally driven by a large increase in natural DIC (Figs. 8c,i and S6c). On the other hand, a cooling in that region tends to decrease surface pCO_2 (Fig. 8k). The simulation also suggests a large non-thermal contribution in the Weddell and Ross Seas. These surface DIC increases correspond to areas with increased mixed layer depth (Fig. S4). The amplitude of the mixed layer depth changes in the Weddell and Ross Seas indicate increased convection, which is also consistent with the simulated increase in AABW (Fig. 7c). The decrease in simulated contemporary pCO_2 trend in the 2000s is associated with a decrease in natural pCO_2 trend (Fig. 8b,h). Similar to observations (Fig. 8f), negative trends occur close to Antarctica and north of 40°S.

The *IAF* simulation and observations however tend to disagree south of 60°S, with *IAF* contemporary pCO_2 not increasing enough in the 1990s and not decreasing enough in the 2000s (Figs. 8 and S6a). Landschützer et al. (2015) suggest that these changes in contemporary pCO_2 south of 60°S mostly arise from the non-thermal trends. In agreement with observations, the *IAF* simulation suggest little changes in the thermal component south of 60°S, indicating that the changes in the non-thermal components are underestimated. An increase in contemporary pCO_2 similar to the one inferred in the SOM-FFN is however simulated in *strong/shift* (Fig. S6b, blue), indicating that either latitudinal changes in the SH westerlies over the 1990s and 2000s are underestimated in *IAF*, or that changes in surface salinity are underestimated.

Over the full period of the *IAF* simulation, the simulated anthropogenic CO_2 fluxes are negatively correlated with SH westerlies (i.e. more carbon uptake as winds strengthen) everywhere in the SO, and particularly between 60°S and 40°S (Fig. 9b). Both contemporary and natural CO_2 fluxes are however positively correlated to changes in the winds south of 50°S, implying a tendency towards CO_2 outgassing with a strengthening of the winds (Fig. 9a,c).

The natural and contemporary CO_2 fluxes however display some zonal differences across the SO. While natural and contemporary CO_2 fluxes are positively correlated with the strength of the SH westerlies in the Atlantic and Indian sectors of the SO, the contrary is simulated in the Pacific (Figs. 9). This asymmetry is mostly due to changes in natural DIC (Fig. S5). This lower surface DIC concentration in the Pacific sector is also associated with a shoaling of the mixed layer depth, whereas the mixed layer depth increases significantly in the Atlantic sector. The negative correlation between natural CO_2 flux and SH westerly wind strength in the Pacific sector of SO may be related to a deepening and/or westward shift of the Amundsen Sea low over the period 1948-2007. A deepening of the Amundsen Sea low has been observed since 1979, and westward shift has been observed for the period 1994-2008 (Turner et al., 2013). This cyclonic circulation over the eastern Pacific sector could explain the relatively higher SST and lower natural surface DIC concentration over that region.

The mixed layer depth increase in the Atlantic sector indicates that there is also enhanced deep-ocean convection in *IAF*. The amplitude of the mixed layer depth increase is however lower in *IAF* compared to *strong/shift* due to weaker and a more equatorward position of the SH westerlies at years 2003-2007 in *IAF*.

3.2.2 Oceanic DIC distribution

We now examine how the distribution of DIC within the oceans has changed in the *IAF* simulation. Observations-based estimates of changes in anthropogenic DIC concentration are available for year 2007 compared to 1994 (Gruber, Clement, et al., 2019) (Fig.

S7b), and are compared to *IAF* for the same years (Fig. S7a). In *IAF* the ocean absorbs 74.8 Gt of anthropogenic carbon between 1970 and 2007. In the SO, anthropogenic DIC concentration is highest in the upper 1000 m, being primarily entrained in AAIW, and SAMW. A minor part of anthropogenic DIC is also entrained in AABW. Simulated and observation-based estimates of anthropogenic DIC concentration anomalies over the period are within 2 mmol/m^3 of each other, with the simulation overestimating the anthropogenic DIC anomalies within AAIW, which could indicate that the simulated AAIW formation rate is slightly overestimated. The observed anthropogenic DIC concentration below 3000 m depth are associated with high uncertainties, thus preventing a model-data comparison.

Over the course of the *IAF* simulation (between 1948 and 2007), there is a 30 mmol/m^3 increase in anthropogenic DIC within SAMW, a 20 mmol/m^3 increase within AAIW and a 2 mmol/m^3 increase within AABW (Fig. 10d-f). There is also a 1 mmol/m^3 increase in anthropogenic DIC spreading in the abyss of the southern Pacific Ocean, associated with AABW. Natural DIC also increases within AAIW (2 mmol/m^3) and SAMW (1 mmol/m^3, Figs. 6, squares and 10a-c), and spread into the Pacific basin. On the other hand, natural DIC decreases below 1000 m depth south of 60°S in both the Atlantic and Pacific sector of SO. These negative DIC anomalies spread in the abyss in the Pacific basin. A $\sim$6 mmol/m^3 decrease in natural DIC is simulated in the deep Atlantic basin, which most likely results from changes in North Atlantic Deep Waters (NADW). As a result, the total DIC concentration increases by only 1 mmol/m^3 within AABW, by 1.5 mmol/m^3 below 1500 m depth in the SO, while the total DIC concentration increases by 19 mmol/m^3 in AAIW and 29 mmol/m^3 within SAMW (Figs. 6, squares and 10g-i). The different patterns in the Atlantic and Pacific basins reflect the different watermasses in these basins with an incursion of NADW in the south Atlantic, and a clear AABW propagation in the abyssal Pacific.

This pattern of lower natural DIC below 1500 m depth in the SO and within AABW, and higher natural DIC within AAIW and SAMW is similar to, while of lower magnitude, than the one simulated in *strong/shift* (Figs. 6 and 10). The responses of the upper and lower overturning cells to a poleward intensification of the SH westerlies as simulated in *IAF* are consistent with the response obtained in CORE-II and CMIP5 models (Downes et al., 2018), and highlight stronger AABW (Fig. 7), with negative natural DIC anomalies spreading into the abyssal Pacific (Fig. 10), little changes within AAIW but reduced subduction of SAMW.

4 Discussion and conclusions

We have used an eddy-permitting global ocean, sea-ice, carbon cycle model to quantify the impact of varying SH westerlies on carbon uptake and oceanic DIC concentrations. These experiments show that as SH westerly winds strengthen the capability of the SO to act as a sink of contemporary carbon reduces. While a poleward shift of the westerlies impact the latitudinal distribution of CO_2 fluxes, the overall effect on SO CO_2 fluxes of stronger westerlies with (*strong/shift*) or without (*strong*) a poleward shift are similar.

As the westerly winds strengthen, the SO upwelling is enhanced, thus increasing the DIC concentration in the mixed layer and reducing the DIC concentration at depth. These changes in SH westerlies are associated with changes in the lower and upper overturning cells, with an increase in both cells as the winds strengthen, while changes in the latitudinal position of the westerlies can lead to asymmetrical changes in the cells. Both a strengthening and poleward shift of the winds lead to a strengthening of AABW formation and subsequent transport at depth, which reduces both the natural and total DIC content within AABW. This is also associated with a 10% strengthening of the ACC, thus enhancing mixing within CDW. As a result, the natural and total DIC decrease within

the SO below 500 m depth, while leading to an increase in surface DIC. This AABW strengthening thus contributes to increased natural CO_2 outgassing (Menviel et al., 2014, 2015). As the SH westerly winds increase, the total DIC concentration decreases within AABW, CDW, and AAIW, but increases within SAMW. Due to a slowdown of the upper cell, a poleward shift of the winds further increases the natural and total DIC concentration within SAMW. However, given that this water mass is shallow and thus upwells back to the surface rapidly, it does not provide an efficient way to increase the oceanic carbon reservoir.

An additional simulation forced with the interannually varying atmospheric forcing (IAF) between 1948 and 2007 provides estimates of SO changes in contemporary, natural and anthropogenic CO_2 fluxes. Our *IAF* simulation displays significant decadal scale variability in total CO_2 fluxes with an amplitude of $\sim$0.2 GtC/yr since 1948 thus supporting previous inferences of decadal scale changes in SO CO_2 fluxes (Li & Ilyina, 2018; Lovenduski et al., 2008; Gruber, Landschützer, & Lovenduski, 2019). The simulated decadal scale changes in total CO_2 fluxes are due to changes in natural CO_2 fluxes primarily arising from changes in the magnitude of the SH westerlies, but also due to changes in latitudinal position of the SH winds. Minimums in total CO_2 uptake arise from a strengthening of the SH winds, while maximum uptakes result from an equatorward shift of the winds.

The mean natural CO_2 flux is relatively constant between 1948 and 1972, while the anthropogenic CO_2 uptake increases, thus leading to an increase in contemporary CO_2 uptake of $\sim$0.5 GtC/yr. From 1972 to 2007 the mean natural CO_2 uptake decreases, and is close to 0 in the early 2000s, due to the strengthening of the SH westerlies and associated enhanced AABW transport. The increase in natural CO_2 outgassing south of 50°S is however compensated by enhanced anthropogenic carbon uptake. The net effect is a stagnation of the contemporary CO_2 uptake in the SO since 1980: as pCO_2 increased between 1980 and 2007 due to anthropogenic emissions, the total oceanic carbon uptake should have also increased, instead it stayed constant. The timing and magnitude of the stagnation in total oceanic carbon uptake in the SO from $\sim$1981 to 2007 is in agreement with observational estimates (Lovenduski et al., 2008; Landschützer et al., 2015; Gruber, Landschützer, & Lovenduski, 2019) and is due to changes in the westerlies. In agreement with previous studies (LeQuéré et al., 2007; Lovenduski et al., 2008; Matear & Lenton, 2008), our results suggest that the slow down of the ocean CO_2 uptake in the 1990s was not due to a lower atmospheric CO_2 growth rate (McKinley et al., 2020), but instead was due to a positive phase of the SAM.

Gruber, Landschützer, and Lovenduski (2019) suggested that the anthropogenic DIC concentration was lower than expected in the intermediate and mode waters of the SO between 1994 and 2007 . Within our modelling framework stronger and poleward shifted SH westerlies in 1990s would have led to positive anthropogenic DIC anomalies in SO watermasses south of 35°S (Fig. 6). Only weaker SH westerlies, or a very large ($\geq$5°) poleward shift of the SH westerlies could reduce the anthropogenic DIC concentration within AAIW and SAMW. Therefore, in agreement with previous studies (Keppler & Landschützer, 2019; Gruber, Landschützer, & Lovenduski, 2019), our modelling work confirm that these observed anthropogenic DIC anomalies are unlikely due to a change in the SH winds.

If SH westerly winds continue to strengthen, as projected under RCP8.5/SSP5-85 scenarios (Grose et al., 2020), our experiments indicate there would be an increase in anthropogenic carbon uptake, but there would also be a greater loss of natural carbon. Future changes in SO carbon uptake will thus result from a fine balance between natural carbon release and anthropogenic carbon uptake, which will itself depend on changes in SH westerlies and SO stratification. In addition, a poleward intensification of the westerlies could also enhance the probability of polynya formation and associated increase in deep-ocean convection. In the 1970's a polynya formed on the Maud Rise, serving as

a precursor to a large polynya in the Weddell Sea (Carsey, 1980). Since then, only in 2017 was another polynya observed on the Maud Rise (Swart et al., 2018), but it did not induce a Weddell Sea polynya due to the relatively low surface salinity at the surface of the Weddell Sea (Cheon & Gordon, 2019). Our idealised *strong/shift* experiment suggests that enhanced deep-ocean convection in the SO could lead to a transient, decadal CO_2 outgassing of up to 1 GtC/yr, primarily through a loss of natural DIC from increased AABW formation.

Acknowledgments

This project was supported by the Australian Research Council. L. Menviel, and P. Spence acknowledge funding from the Australian Research Council grants FT180100606 and FT190100413. Experiments were performed on Raijin at NCI with support from the National Computational Merit Allocations Scheme (NCMAS).

Data availability Results of the modelling experiments have been submitted to Research Data Australia: $https://doi.org/10.26190/5f31f0318a5c8$

References

Carsey, F. (1980). Microwave Observation of the Weddell Polynya. *Monthly weather review*, *108*, 2032-2044.

Cheon, W., & Gordon, A. (2019). Open-ocean polynyas and deep convection in the Southern Ocean. *Scientific Reports*, *9*. doi: 10.1038/s41598-019-43466-2

Downes, S., C., L., Brook, J. P., & P., S. (2017). Regional Impacts of the Westerly Winds on Southern Ocean Mode and Intermediate Water Subduction. *Journal of Physical Oceanography*, *47*(10), 2521 - 2530. doi: 10.1175/JPO-D-17-0106.1

Downes, S., Spence, P., & Hogg, A. (2018). Understanding variability of the Southern Ocean overturning circulation in CORE-II models. *Ocean Modelling*, *123*, 98 - 109. Retrieved from `http://www.sciencedirect.com/science/article/pii/S1463500318300234` doi: https://doi.org/10.1016/j.ocemod.2018.01.005

Dufour, C. O., Sommer, J. L., Gehlen, M., Orr, J. C., Molines, J.-M., Simeon, J., & Barnier, B. (2013). Eddy compensation and controls of the enhanced sea-to-air CO2 flux during positive phases of the Southern Annular Mode. *Global Biogeochemical Cycles*, *27*(3), 950-961. Retrieved from `https://agupubs.onlinelibrary.wiley.com/doi/abs/10.1002/gbc.20090` doi: https://doi.org/10.1002/gbc.20090

Farneti, R., Downes, S., Griffies, S., Marsland, S., Behrens, E., Bentsen, M., ... Yeager, S. (2015). An assessment of Antarctic Circumpolar Current and Southern Ocean meridional overturning circulation during 1958-2007 in a suite of interannual CORE-II simulations. *Ocean Model.*, *93*, 84-120.

Fogt, R. L., & Marshall, G. J. (2020). The Southern Annular Mode: Variability, trends, and climate impacts across the Southern Hemisphere. *WIREs Climate Change*, *11*(4), e652. Retrieved from `https://onlinelibrary.wiley.com/doi/abs/10.1002/wcc.652` doi: https://doi.org/10.1002/wcc.652

Gloege, L., McKinley, G. A., Landschtzer, P., Fay, A. R., Frlicher, T. L., Fyfe, J. C., ... Takano, Y. (2021). Quantifying errors in observationally based estimates of ocean carbon sink variability. *Global Biogeochemical Cycles*, *35*(4), e2020GB006788. Retrieved from `https://agupubs.onlinelibrary.wiley.com/doi/abs/10.1029/2020GB006788` doi: https://doi.org/10.1029/2020GB006788

Gray, A. R., Johnson, K. S., Bushinsky, S. M., Riser, S. C., Russell, J. L., Talley, L. D., ... Sarmiento, J. L. (2018). Autonomous Biogeochemical Floats Detect Significant Carbon Dioxide Outgassing in the High-Latitude Southern Ocean. *Geophysical Research Letters*, *45*(17), 9049-9057. Retrieved from `https://agupubs.onlinelibrary.wiley.com/doi/abs/10.1029/2018GL078013` doi: https://doi.org/10.1029/2018GL078013

Griffies, S. (2012). *Elements of the modular ocean model (mom): 2012 release (gfdl ocean group technical report no. 7)* (Tech. Rep.). NOAA/Geophysical Fluid Dynamics Laboratory, Princeton, USA.

Griffies, S., Biastoch, A., Boning, C., Bryan, F., Danabasoglu, G., Chassignet, E., ... Yin, J. (2009). Coordinated Ocean-ice Reference Experiments (COREs). *Ocean Model.*, *26*, 1-46.

Grose, M. R., Narsey, S., Delage, F. P., Dowdy, A. J., Bador, M., Boschat, G., ... Power, S. (2020). Insights From CMIP6 for Australia's Future Climate. *Earth's Future*, *8*(5), e2019EF001469. Retrieved from `https://agupubs.onlinelibrary.wiley.com/doi/abs/10.1029/2019EF001469` doi: 10.1029/2019EF001469

Gruber, N., Clement, D., Carter, B. R., Feely, R. A., van Heuven, S., Hoppema, M., ... Wanninkhof, R. (2019). The oceanic sink for anthropogenic CO2 from 1994 to 2007. *Science*, *363*(6432), 1193–1199. Retrieved from `http://science.sciencemag.org/content/363/6432/1193` doi: 10.1126/science.aau5153

Gruber, N., Landschützer, P., & Lovenduski, N. (2019). The variable Southern Ocean carbon sink. *Annual Review of Marine Science*, *11*, 159-186.

Hauck, J., Vlker, C., Wang, T., Hoppema, M., Losch, M., & Wolf-Gladrow, D. A. (2013). Seasonally different carbon flux changes in the southern ocean inresponse to the southern annular mode. *Global Biogeochemical Cycles*, *27*(4), 1236-1245. Retrieved from https://agupubs.onlinelibrary.wiley.com/doi/abs/10.1002/2013GB004600 doi: https://doi.org/10.1002/2013GB004600

Hofmann, M., & Maqueda, M. M. (2011). The response of Southern Ocean eddies to increased midlatitude westerlies: A non-eddy resolving model study. *Geophys. Res. Lett.*, *38*, doi:10.1029/2010GL045972.

Hogg, A., Spence, P., Saenko, O., & Downes, S. (2017). The Energetics of Southern Ocean Upwelling. *J. Phys. Oceanogr.*, *47*, 135-153.

Joos, F., & Spahni, R. (2008). Rates of change in natural and anthropogenic radiative forcing over the past 20,000 years. *Proceedings of the National Academy of Sciences*, *105*(5), 1425–1430. Retrieved from https://www.pnas.org/content/105/5/1425 doi: 10.1073/pnas.0707386105

Keppler, L., & Landschützer, P. (2019). Regional Wind Variability Modulates the Southern Ocean Carbon Sink. *Sci. Rep.*, *7384*. doi: 10.1038/s41598-019-43826-y

Kidston, M., Matear, R., & Baird, M. (2011). Parameter optimisation of a marine ecosystem model at two contrasting stations in the Sub-Antarctic Zone. *Deep-Sea Research II*, *58*, 2301-2315.

Landschützer, P., Gruber, N., & Bakker, D. C. E. (2016). Decadal variations and trends of the global ocean carbon sink. *Global Biogeochemical Cycles*, *30*. doi: 10.1002/2015GB005359

Landschützer, P., Gruber, N., Haumann, F. A., Rödenbeck, C., Bakker, D. C. E., van Heuven, S., ... Wanninkhof, R. (2015). The reinvigoration of the Southern Ocean carbon sink. *Science*, *349*(6253), 1221–1224. Retrieved from http://science.sciencemag.org/content/349/6253/1221 doi: 10.1126/science.aab2620

Large, W., & Yeager, S. (2009). The global climatology of an interannually varying air-sea flux data set. *Clim. Dyn.*, *33*, 341-364.

Lauderdale, J. M., Garabato, A. C. N., Oliver, K. I. C., Follows, M. J., & Williams, R. G. (2013). Wind-driven changes in Southern Ocean residual circulation, ocean carbon reservoirs and atmospheric CO_2. *Climate Dynamics*, *41*(7), 2145–2164. doi: 10.1007/s00382-012-1650-3

Lauderdale, J. M., Williams, R. G., Munday, D. R., & Marshall, D. P. (2017, Mar 01). The impact of Southern Ocean residual upwelling on atmospheric CO2 on centennial and millennial timescales. *Climate Dynamics*, *48*(5), 1611–1631. Retrieved from https://doi.org/10.1007/s00382-016-3163-y doi: 10.1007/s00382-016-3163-y

Law, R. M., Ziehn, T., Matear, R. J., Lenton, A., Chamberlain, M. A., Stevens, L. E., ... Vohralik, P. F. (2017). The carbon cycle in the Australian Community Climate and Earth System Simulator (ACCESS-ESM1) – Part 1: Model description and pre-industrial simulation. *Geoscientific Model Development*, *10*, 2567-2590. doi: 10.5194/gmd-10-2567-2017

Lenton, A., & Matear, R. (2007). Role of the Southern Annular Mode (SAM) in Southern Ocean CO_2 uptake. *Global Biogeochemical Cycles*, *21*, doi:10.1029/2006GB002714.

Le Quéré, C., Andrew, R. M., Friedlingstein, P., Sitch, S., Pongratz, J., Manning, A. C., ... Zhu, D. (2018). Global Carbon Budget 2017. *Earth System Science Data*, *10*(1), 405–448. Retrieved from https://www.earth-syst-sci-data.net/10/405/2018/ doi: 10.5194/essd-10-405-2018

LeQuéré, C., Rödenbeck, C., Buitenhuis, E., Conway, T., Langenfelds, R., Gomez,

A., ... Heimann, M. (2007). Saturation of the Southern Ocean CO_2 sink due to recent climate change. *Science*, *316*, 1735-1738.

Li, H., & Ilyina, T. (2018). Current and future decadal trends in the oceanic carbon uptake are dominated by internal variability. *Geophysical Research Letters*, *45*(2), 916-925. Retrieved from `https://agupubs.onlinelibrary.wiley.com/doi/abs/10.1002/2017GL075370` doi: 10.1002/2017GL075370

Lovenduski, N., Gruber, N., & Doney, S. (2008). Toward a mechanistic understanding of the decadal trends in the Southern Ocean carbon sink. *Global Biogeochemical Cycles*, *22*, doi:10.1029/2007GB003139.

Lovenduski, N., Gruber, N., Doney, S., & Lima, I. (2007). Enhanced CO_2 outgassing in the Southern Ocean from a positive phase of the Southern Annular Mode. *Global Biogeochemical Cycles*, *21*, doi:10.1029/2006GB002900.

Marshall, G. (2003). Trends in the Southern Annular Mode from observations and reanalyses. *J. Clim.*, *16*, 4134-4143.

Matear, R., & Lenton, A. (2008). Impact of Historical Climate Change on the Southern Ocean Carbon Cycle. *Journal of Climate*, *21*(22), 5820-5834. doi: 10.1175/2008JCLI2194.1

McKinley, G. A., Fay, A. R., Eddebbar, Y. A., Gloege, L., & Lovenduski, N. S. (2020). External Forcing Explains Recent Decadal Variability of the Ocean Carbon Sink. *AGU Advances*, *1*(2), e2019AV000149. Retrieved from `https://agupubs.onlinelibrary.wiley.com/doi/abs/10.1029/2019AV000149` (e2019AV000149 2019AV000149) doi: https://doi.org/10.1029/2019AV000149

Menviel, L., England, M., Meissner, K., Mouchet, A., & Yu, J. (2014). Atlantic-Pacific seesaw and its role in outgassing CO_2 during Heinrich events. *Paleoceanography*, *29*, 58-70. doi: 10.1002/2013PA002542

Menviel, L., Mouchet, A., Meissner, K., Joos, F., & England, M. (2015). Impact of oceanic circulation changes on atmospheric $\delta^{13}CO_2$. *Global Biogeochemical Cycles*, *29*, 1944-1961. doi: 10.1002/2015GB005207

Menviel, L., Spence, P., Yu, J., Chamberlain, M., Matear, R., Meissner, K., & England, M. (2018). Southern Hemisphere westerlies as a driver of the early deglacial atmospheric CO_2 rise. *Nature Communications*, *9*, 2503. doi: 10.1038/s41467-018-04876-4

Menviel, L., Timmermann, A., Mouchet, A., & Timm, O. (2008). Climate and marine carbon cycle response to changes in the strength of the southern hemispheric westerlies. *Paleoceanography*, *23*, doi:10.1029/2007PA001604.

Mikaloff-Fletcher, S., Gruber, N., Jacobson, A., Doney, S., Dutkiewicz, S., Gerber, M., ... Sarmiento, J. (2006). Inverse estimates of anthropogenic CO_2 uptake, tranport, and storage by the ocean. *Global Biogeochemical Cycles*, *20*, GB2002. doi: 10.1029/2005GB002530

Munday, D. R., Johnson, H. L., & Marshall, D. P. (01 Mar. 2013). Eddy Saturation of Equilibrated Circumpolar Currents. *Journal of Physical Oceanography*, *43*(3), 507 - 532. Retrieved from `https://journals.ametsoc.org/view/journals/phoc/43/3/jpo-d-12-095.1.xml` doi: 10.1175/JPO-D-12-095.1

Munday, D. R., Johnson, H. L., & Marshall, D. P. (2014). Impacts and effects of mesoscale ocean eddies on ocean carbon storage and atmospheric pCO2. *Global Biogeochemical Cycles*, *28*(8), 877-896. Retrieved from `https://agupubs.onlinelibrary.wiley.com/doi/abs/10.1002/2014GB004836` doi: 10.1002/2014GB004836

Oke, P., Griffin, D., Schiller, A., Matear, R., Fiedler, R., Mansbridge, J., ... Ridgway, K. (2013). Evaluation of a near-global eddy-resolving ocean model. *Geoscience Model Development*, *6*, 591–615. doi: 10.5194/gmd-6-591-2013

Olsen, A., Key, R. M., van Heuven, S., Lauvset, S. K., Velo, A., Lin, X., ... Suzuki., T. (2016). The Global Ocean Data Analysis Project version 2 (GLODAPv2) - an internally consistent data product for the world ocean. *Earth System Science Data*, *8*, 297-323.

Ritter, R., Landschtzer, P., Gruber, N., Fay, A. R., Iida, Y., Jones, S., ... Zeng, J. (2017). Observation-Based Trends of the Southern Ocean Carbon Sink. *Geophysical Research Letters*, *44*(24), 12,339-12,348. Retrieved from `https://agupubs.onlinelibrary.wiley.com/doi/abs/10.1002/2017GL074837` doi: https://doi.org/10.1002/2017GL074837

Sabine, C., Feely, R., Gruber, N., Key, R., Lee, K., Bullister, J., ... Rios, A. (2004). The oceanic sink of anthropogenic CO_2. *Science*, *305*, 367-371.

Sarmiento, J., & Gruber, N. (2006). *Ocean biogeochemical dynamics* (Vol. 526pp). Princeton University Press, Princeton, NJ.

Sinha, A., & Abernathy, R. (2016). Time Scales of Southern Ocean Eddy Equilibration. *J. Phys. Ocean*, *46*(9), 2785-2805. doi: https://doi.org/10.1175/JPO-D-16-0041.1

Spence, P., Griffies, S. M., England, M. H., Hogg, A. M., Saenko, O. A., & Jourdain, N. C. (2014). Rapid subsurface warming and circulation changes of antarctic coastal waters by poleward shifting winds. *Geophysical Research Letters*, *41*(13), 4601-4610. Retrieved from `https://agupubs.onlinelibrary.wiley.com/doi/abs/10.1002/2014GL060613` doi: 10.1002/2014GL060613

Spence, P., Holmes, R., Hogg, A., Griffies, S., Stewart, K., & England, M. (2017). Localized rapid warming of West Antarctic subsurface waters by remote winds. *Nature Climate Change*, *7*, 595-603.

Swart, N., Gille, S., & et al., J. F. (2018). Recent Southern Ocean warming and freshening driven by greenhouse gas emissions and ozone depletion. *Nature Geoscience*, *11*, 836-841.

Toggweiler, J. (1999). Variation of atmospheric CO_2 by ventilation of the ocean's deepest water. *Paleoceanography*, *14*, 571-588.

Turner, J., Phillips, T., Hosking, J. S., Marshall, G. J., & Orr, A. (2013). The amundsen sea low. *International Journal of Climatology*, *33*(7), 1818-1829. Retrieved from `https://rmets.onlinelibrary.wiley.com/doi/abs/10.1002/joc.3558` doi: https://doi.org/10.1002/joc.3558

Völker, C., & Köhler, P. (2013). Responses of ocean circulation and carbon cycle to changes in the position of the Southern Hemisphere westerlies at Last Glacial Maximum. *Paleoceanography*, *28*, 726-739. doi: 10.1002/2013PA002556

Wanninkhof, R. (1992). Relationship between gas exhange and wind speed over the ocean. *Journal of Geophysical Research*, *97*, 7373-7381.

Waugh, D. W., McC. Hogg, A., Spence, P., England, M. H., & Haine, T. W. N. (2019). Response of southern ocean ventilation to changes in midlatitude westerly winds. *Journal of Climate*, *32*(17), 5345-5361. Retrieved from `https://doi.org/10.1175/JCLI-D-19-0039.1` doi: 10.1175/JCLI-D-19-0039.1

Zheng, F., Li, J., Clark, R., & Nnamchi, H. (2013). Simulation and Projection of the Southern Hemisphere Annular Mode in CMIP5 Models. *Journal of Climate*, *26*, 9860-9879. doi: 10.1175/JCLI-D-13-00204.1

Ziehn, T., Chamberlain, M. A., Law, R. M., Lenton, A., Bodman, R. W., Dix, M., ... Srbinovsky, J. (2020). The australian earth system model: Access-esm1.5. *Journal of Southern Hemisphere Earth Systems Science*. doi: 10.1071/ES19035

Experiment	Atm. forcing	SO τ (N/m^2)	Lat. of max τ
IAF	CORE IAF v.2	0.09 in 1948-1952	49°S
		0.12 in 1970-1974	52°S
		0.13 in 2003-2007	52.5°S
control	CORE NYF v.2	0.12	52°S
weak	CORE NYF v.2	0.08	52°S
strong	CORE NYF v.2	0.17	52°S
strong/shift	CORE NYF v.2	0.17	56°S

Table 1. Atmospheric forcing, mean strength (averaged over 58°S-40°) and latitude of maximum SO (SO) windstress (τ) in the experiments performed.

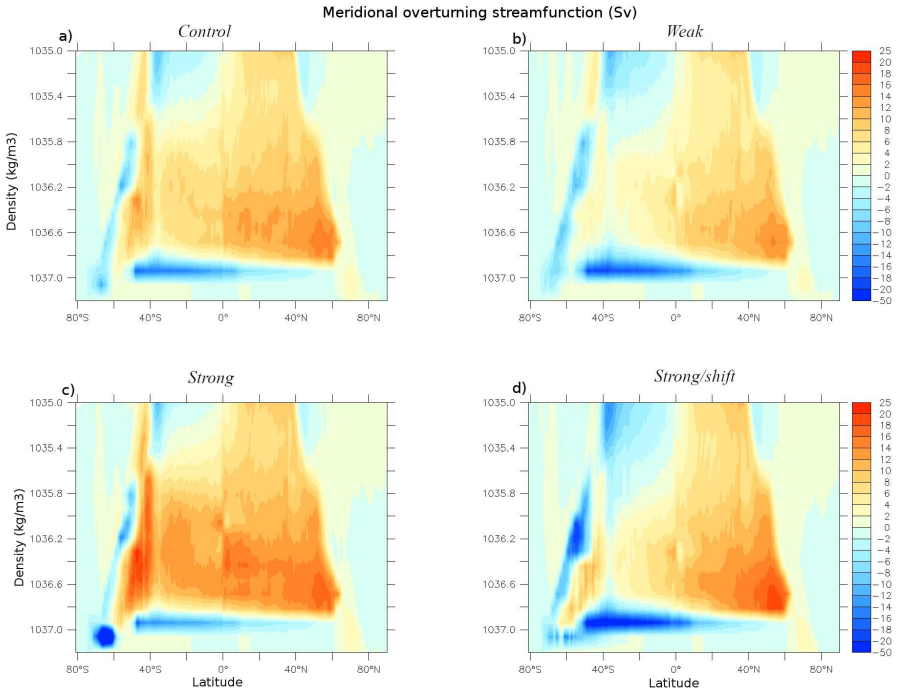

Figure 1. Overturning in density space for **a)** *control*, **b)** *weak*, **c)** *strong* and **d)** *strong/shift*. Here density is calculated relative to 2000 m reference depth. AABW is at $\sigma \geq 1037$ kg/m^3, and AAIW at $1036 > \sigma > 1036.5$ kg/m^3.

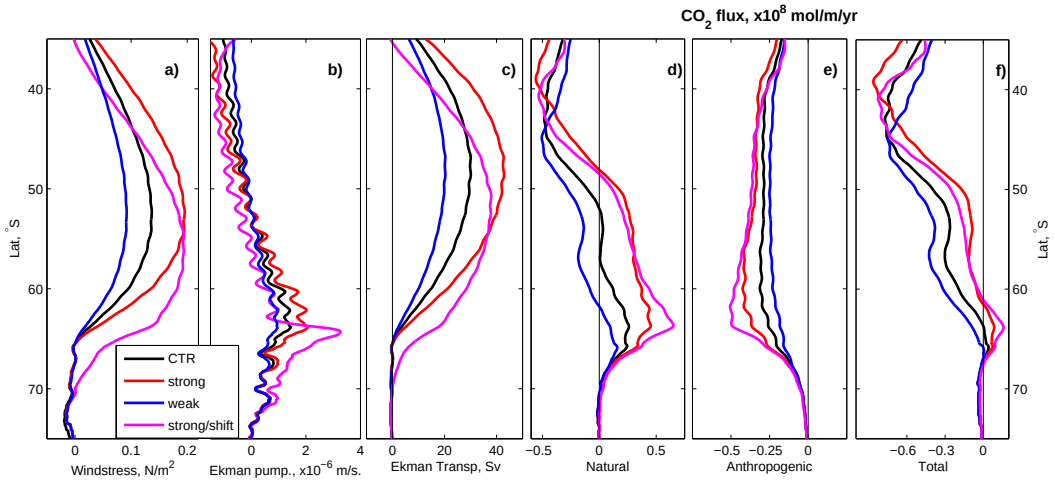

Figure 2. Zonally averaged **a)** zonal windstress (N/m^2); **b)** upward Ekman pumping (m/s); **c)** northward Ekman transport (Sv); Zonally integrated CO_2 fluxes (x10^8 mol/m/yr) in **d)** natural carbon, **e)** anthropogenic carbon, and **f)** total carbon. for the (black) *control*, (red) *strong*, (blue) *weak* and (magenta) *strong/shift* experiments averaged over years 2007-2011. Negative values indicate an ocean CO_2 uptake and positive oceanic CO_2 outgassing.

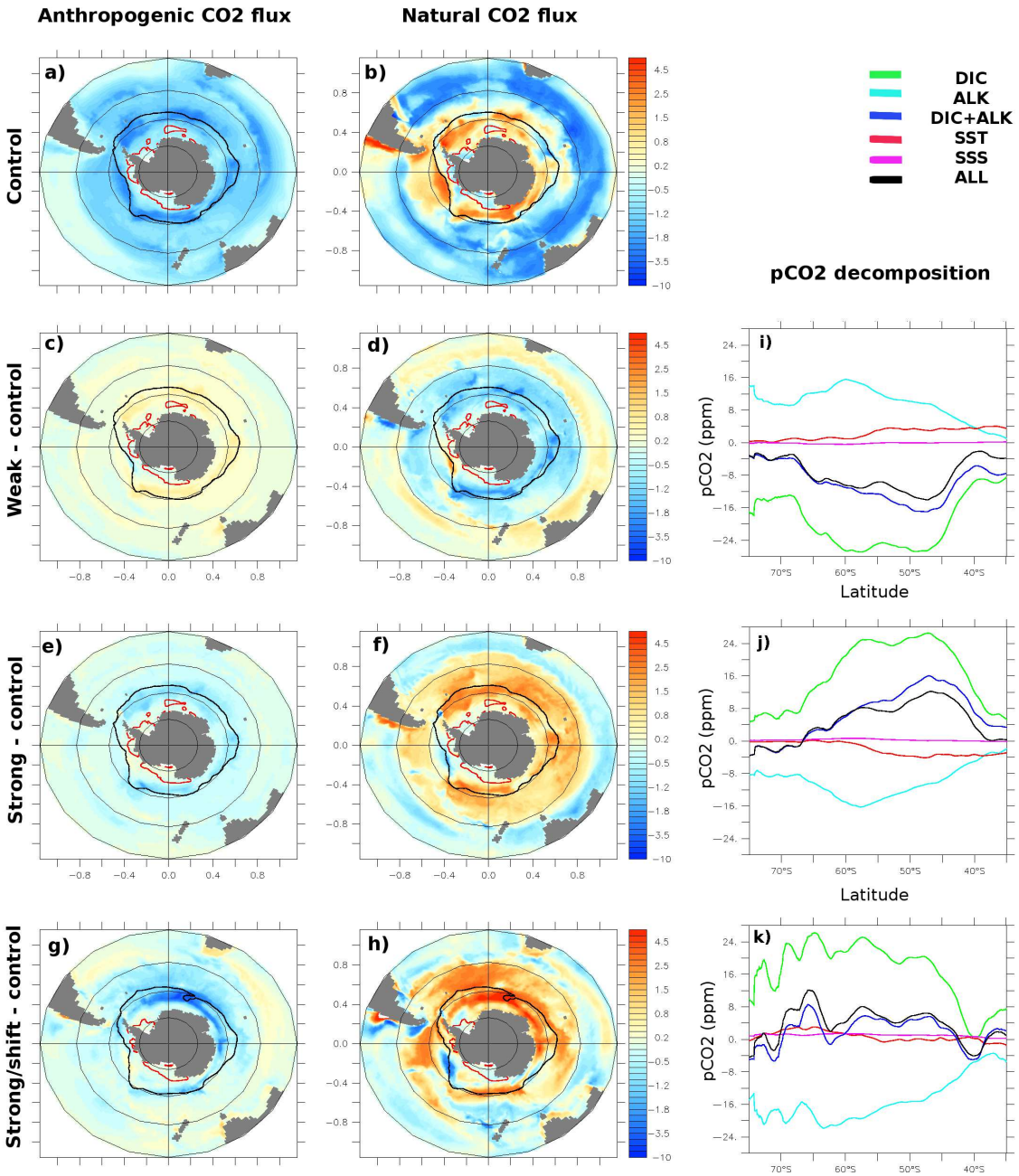

Figure 3. (left) Anthropogenic and (middle) natural CO_2 flux out of the ocean (mol/m^2/yr) for **a,b)** the control run; **c,d)** *weak*, **e,f)** *strong* and **g,h)** *strong/shift* compared to *control* for years 2007-2011. The 15% sea-ice concentration contour for September (black) and March (red) are shown for each experiment. Positive anomalies indicate stronger CO_2 outgassing or reduced CO_2 uptake. (right) Zonally averaged DIC (green), alkalinity (cyan), SST (red), SSS (magenta) contributions to the natural oceanic pCO_2 anomalies (ppm) for **i)** *weak*, **j)** *strong* and **k)** *strong/shift* compared to *control* for years 2007-2011. The combined DIC plus alkalinity contributions are in blue and the sum of all the contributions in black.

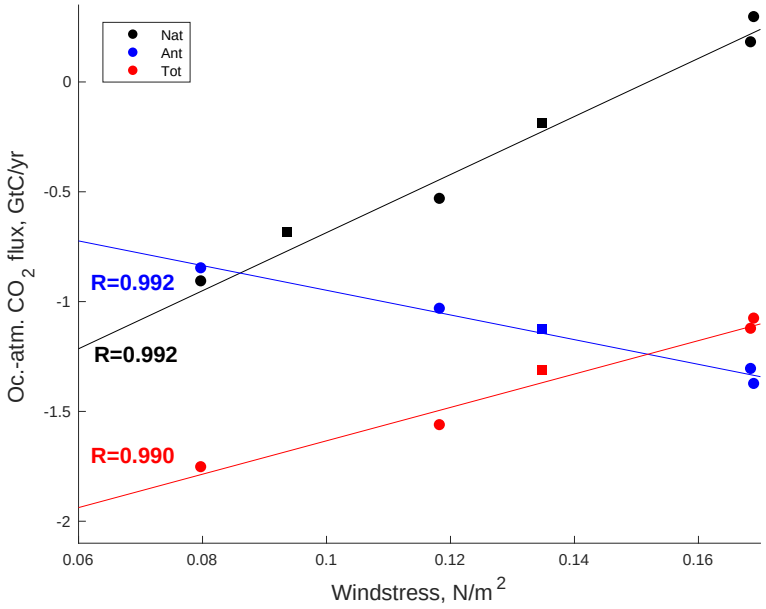

Figure 4. Relationship between mean SO windstress and integrated CO_2 flux south of 35°S for natural (black), anthropogenic (blue), and total carbon (red) for all experiments averaged over years 1998-2002. *IAF* averaged over years 1948-1953 is also included for the natural CO_2 flux, but not for the anthropogenic and total CO_2 fluxes, as the contemporary atmospheric CO_2 concentration was different. Negative values indicate oceanic CO_2 uptake. The squares indicate the *IAF* at years 1948-1953 and 1998-2002.

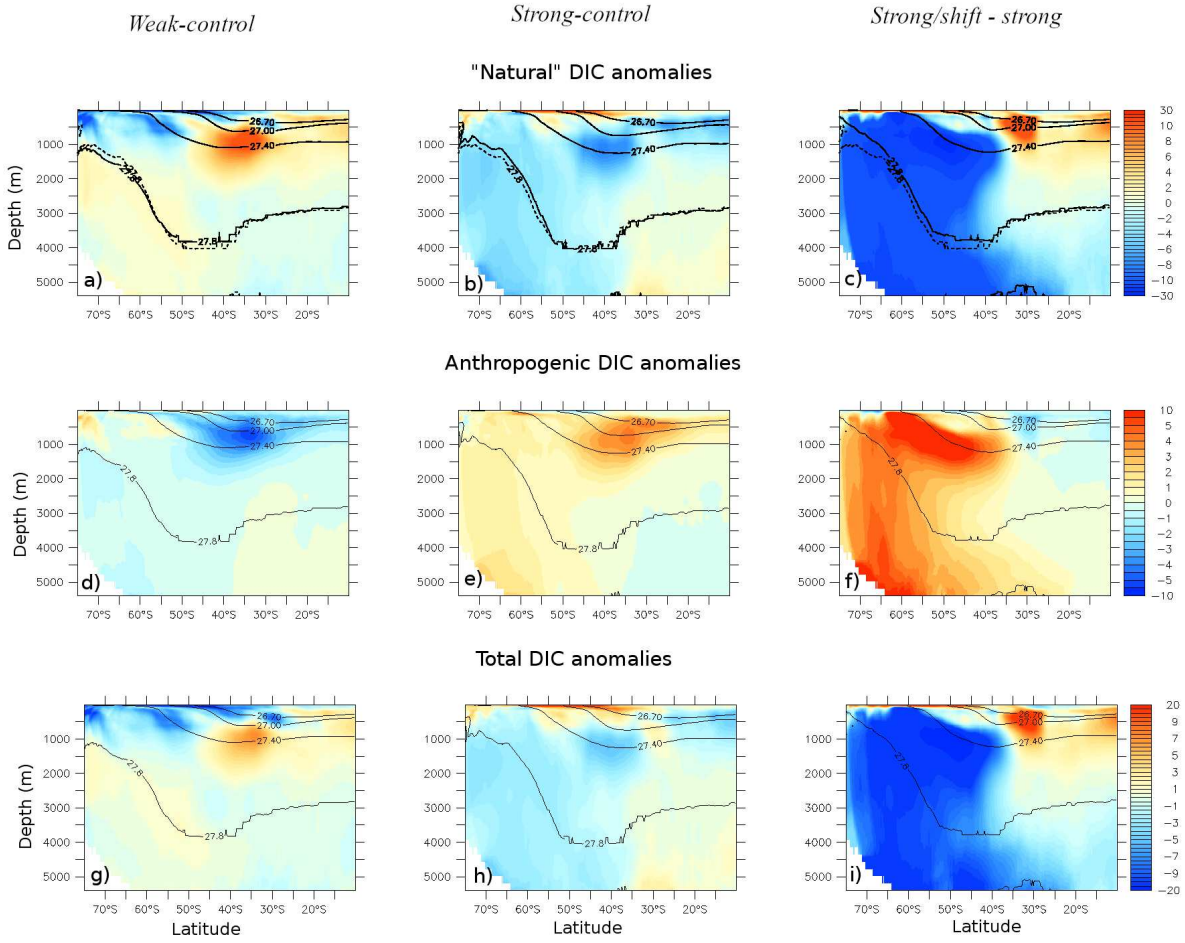

Figure 5. Zonally averaged DIC anomalies (mmol/m^3) averaged over years 2007-2011 for (left) *weak*, and (middle) *strong* compared to *control*, and (right) for *strong/shift* compared to *strong* for (top) natural DIC, (middle) anthropogenic DIC and (bottom) total DIC. The potential density lines delimiting AABW ($\sigma > 27.75 kg/m^3$), AAIW (27.4 > σ >27 kg/m^3), and SAMW (27 > σ >26.7 kg/m^3) for the sensitivity experiments (solid lines), and the 27.75 kg/m^3 for the control (dashed lines).

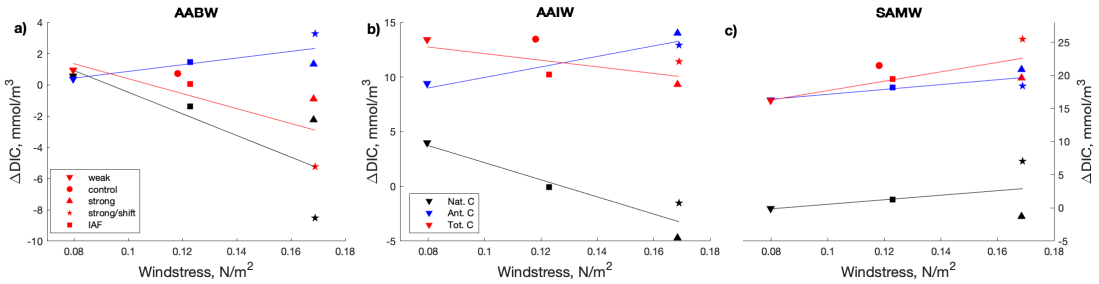

Figure 6. Changes in DIC concentration (mmol/m^3) within **a)** AABW, **b)** AAIW, and **c)** SAMW for natural DIC (black), anthropogenic DIC (blue) and total DIC (red) for experiments *weak* (downward triangle), *control* (circle), *strong* (upward triangle), *strong/shift* (star) and *IAF* (square). Anomalies are averages of years 2003-2007 compared to years 1970-1974 of *control* for *weak*, *strong*, *strong/shift* and *control*. For *IAF* anomalies represent years 2003-2007 compared to *IAF* years 1970-1974, and the windstress refers to the mean windstress over the period 1970-2007. Solid lines represent trends with windstress within each watermass and for natural DIC (black), anthropogenic DIC (blue) and total DIC (red).

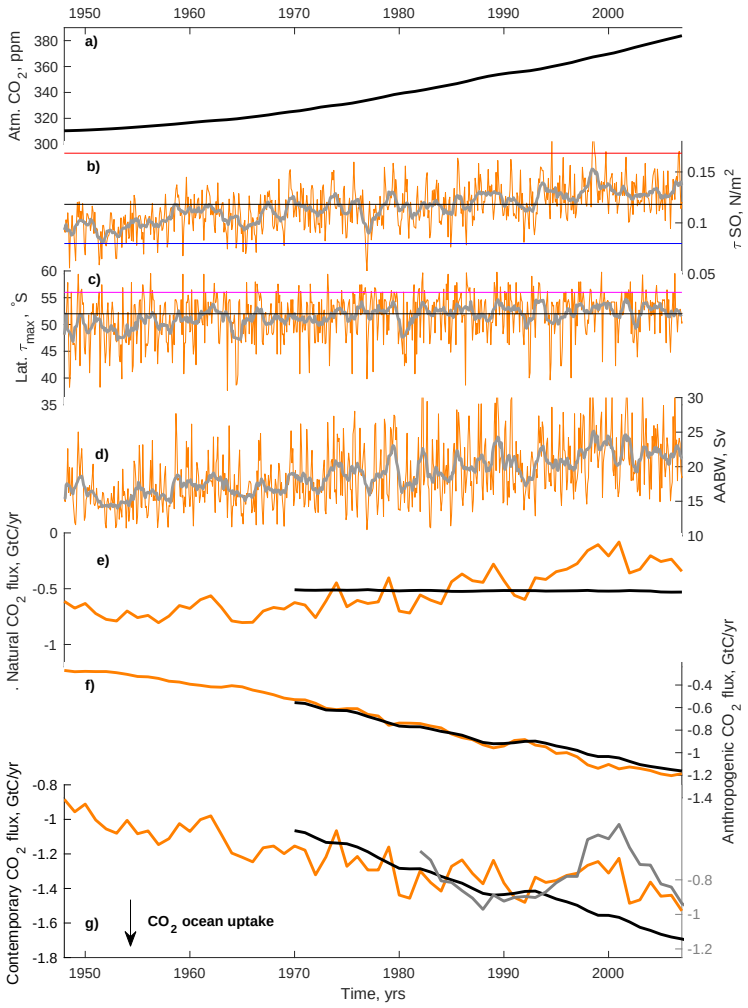

Figure 7. Time series of **a)** atmospheric CO_2 concentration (ppm) used as a forcing for the anthropogenic carbon tracer; **b)** SO windstress averaged over 58°S-40°S; **c)** Latitude (°S) of the maximum SO windstress; **d)** AABW transport, defined as the minimum overturning streamfunction in the deep ocean south of 20°S; Integrated ocean-air CO_2 flux (GtC/yr) south of 35°S for **e)** natural, **f)** anthropogenic, and **g)** total carbon for (orange) the IAF run compared to (grey) observational estimates as inferred from the SOM-FFN (Landschützer et al., 2016). The control run is shown in black for comparison. Negative values indicate an ocean CO_2 uptake and positive oceanic CO_2 outgassing. The black, blue, red horizontal and magenta lines in b) and c) show the SO windstress in experiments *control*, *weak*, *strong* and *strong/shift*, respectively.

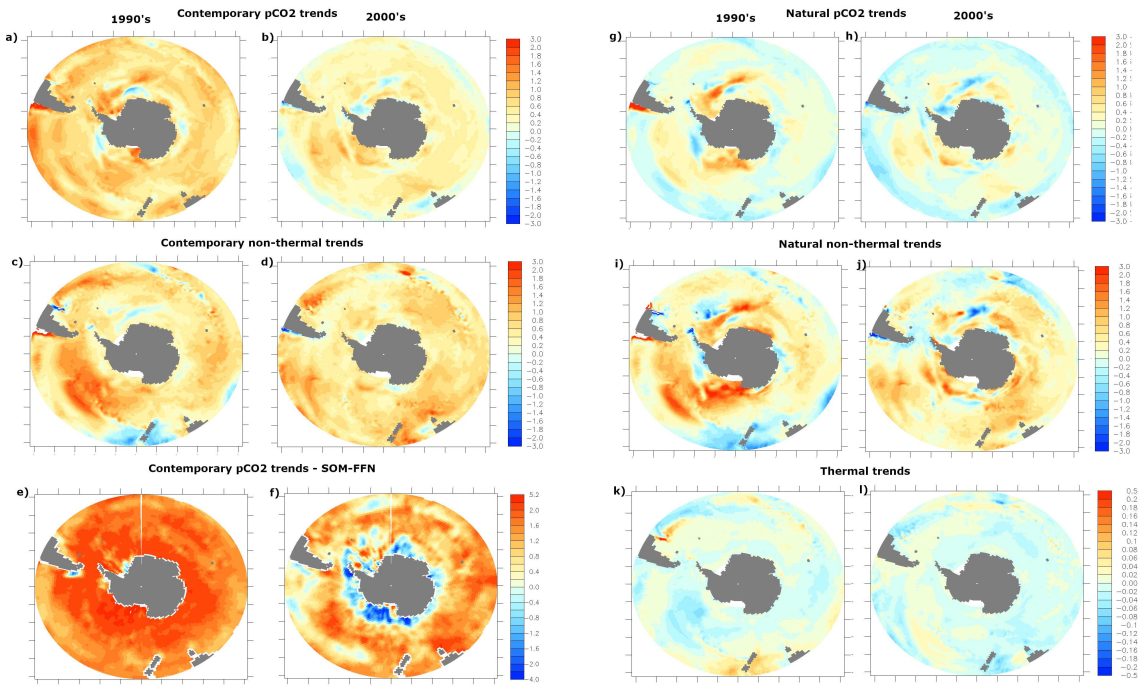

Figure 8. **a, b)** Surface contemporary pCO_2 trends (ppm/yr) as simulated in *IAF* and **c, d)** the non-thermal contribution to contemporary pCO_2 trends (ppm/yr). **e, f)** Surface contemporary pCO_2 trends (ppm/yr) as estimated from the SOM-FFN **a, c, e)** between years 1992 and 2001 and **b,d,f)** between years 2001 and 2006; **g,h)** Surface natural pCO_2 trends (ppm/yr) as simulated in *IAF*, **i, j)** non-thermal contribution to natural pCO_2 trends (ppm/yr), and **k, l)** thermal contribution to natural pCO_2 trends (ppm/yr) **g,i,k)** between years 1992 and 2001 and **h,j,l)** between years 2001 and 2006.

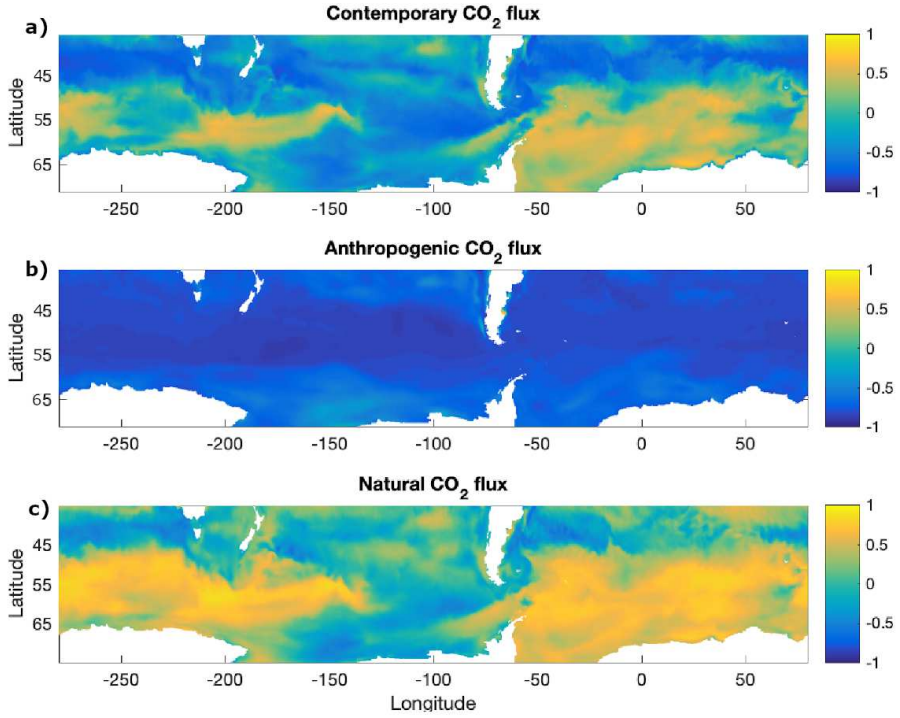

Figure 9. (left) Correlations between CO_2 fluxes as simulated in *IAF* and SH westerlies over the full period of the simulation (1948-2007) for **a)** contemporary, **b)** anthropogenic and **c)** natural CO_2 fluxes.

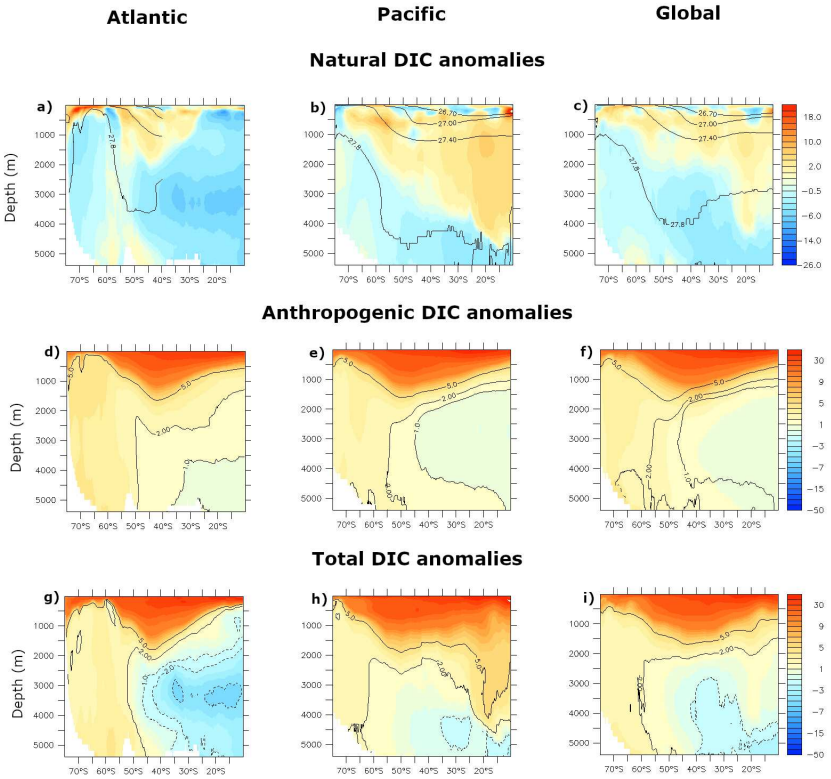

Figure 10. Zonally averaged DIC anomalies (mmol/m^3) as simulated in *IAF* for years 2003-2007 compared to years 1948-1952 averaged over **a, d, g)** the Atlantic Ocean, **b, e, h)** the Pacific Ocean, and **c, f, i)** the global ocean and for for **a-c)** natural DIC, **d-f)** anthropogenic DIC and **g-i)** total DIC. The potential density lines delimiting AABW (σ >27.75 kg/m^3), AAIW (27.4 > σ >27 kg/m^3), and SAMW (27 > σ >26.7 kg/m^3) (solid lines) are shown.

Figure 1.

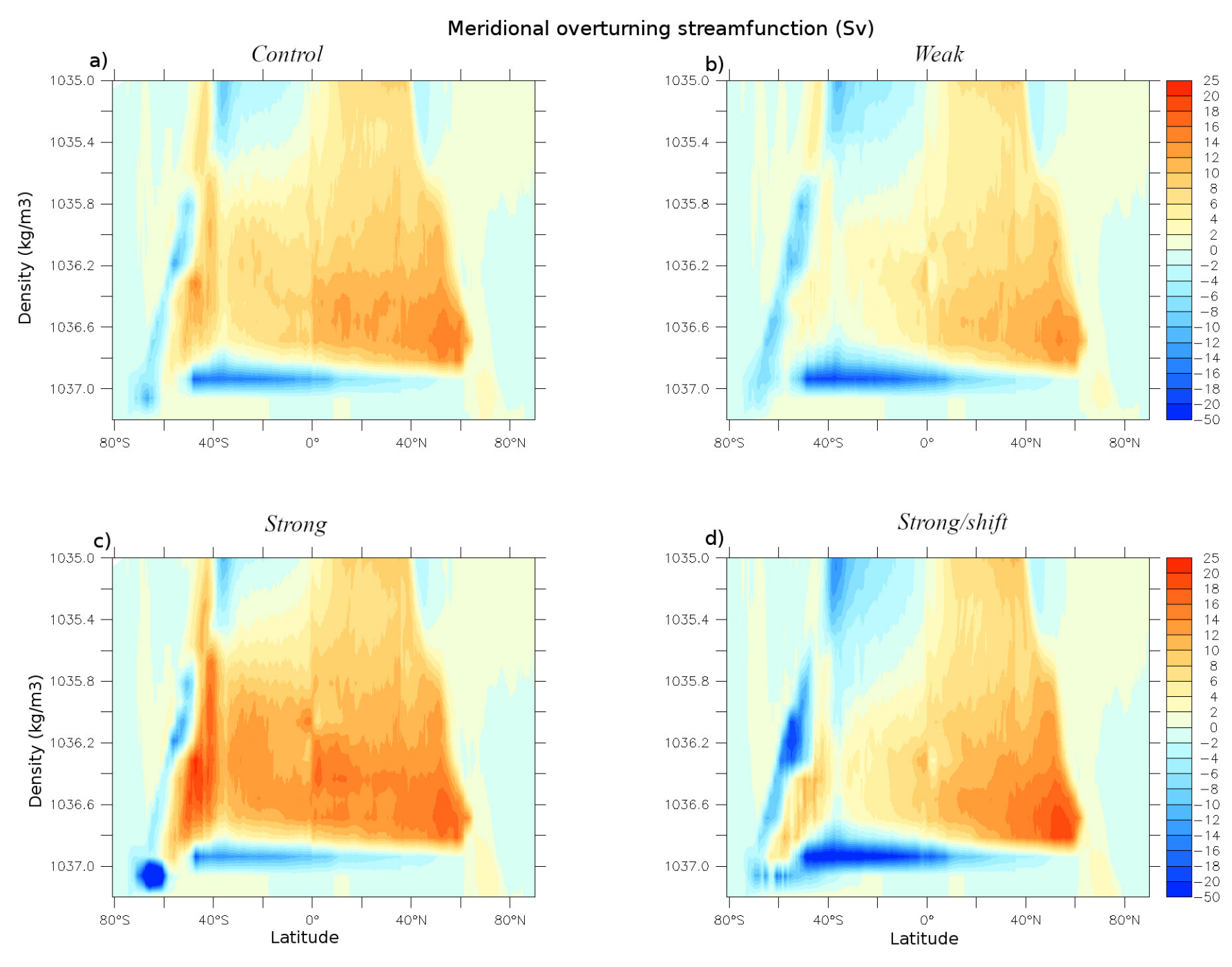
Meridional overturning streamfunction (Sv)
a)
Control
b)
Weak
c)
Strong
d)
Strong/shift
Density (kg/m3)
1035.0
1035.4
1035.8
1036.2
1036.6
1037.0
80°S
40°S
0°
40°N
80°N
Latitude
25
20
18
16
14
12
10
8
6
4
2
0
−2
−4
−6
−8
−10
−12
−14
−16
−18
−20
−50

Figure 2.

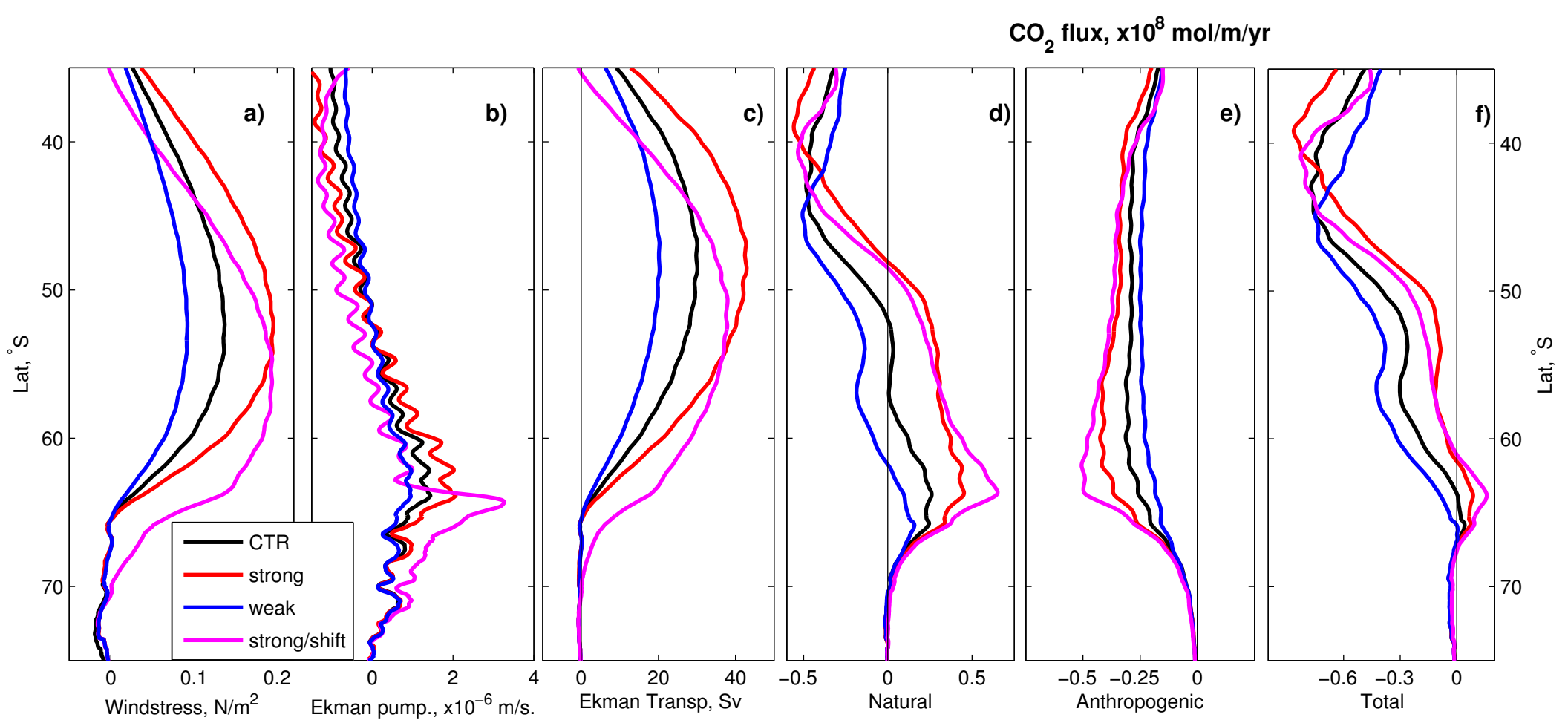
CO2 flux, x10^8 mol/m/yr
a)
b)
c)
d)
e)
f)
Lat, °S
40
50
60
70
CTR
strong
weak
strong/shift
0
0.1
0.2
Windstress, N/m2
0
2
4
Ekman pump., x10−6 m/s.
0
20
40
Ekman Transp, Sv
−0.5
0
0.5
Natural
−0.5
−0.25
0
Anthropogenic
−0.6
−0.3
0
Total

Figure 3.

Anthropogenic CO2 flux

Natural CO2 flux

Control

Weak - control

Strong - control

Strong/shift - control

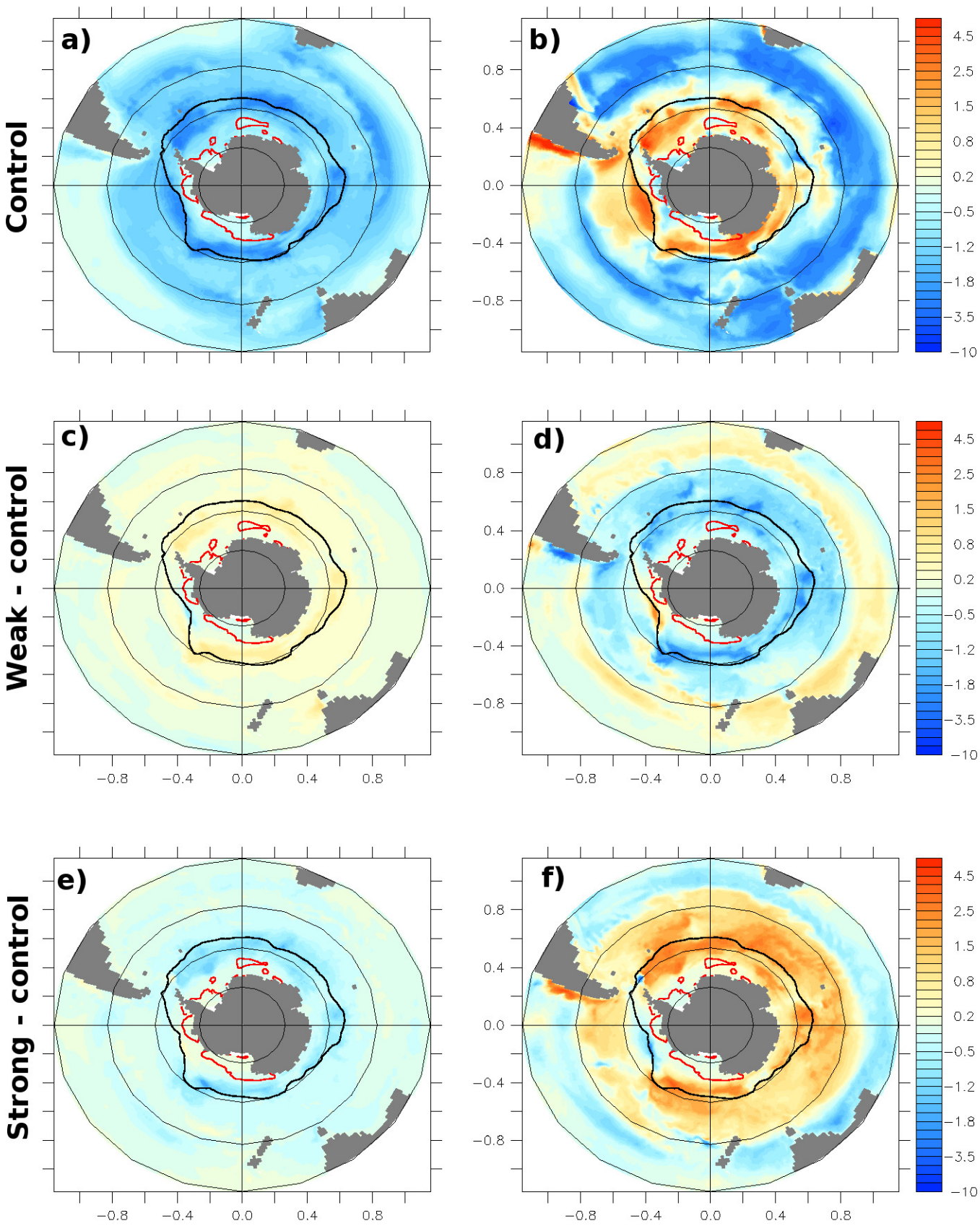

DIC
ALK
DIC+ALK
SST
SSS
ALL

pCO2 decomposition

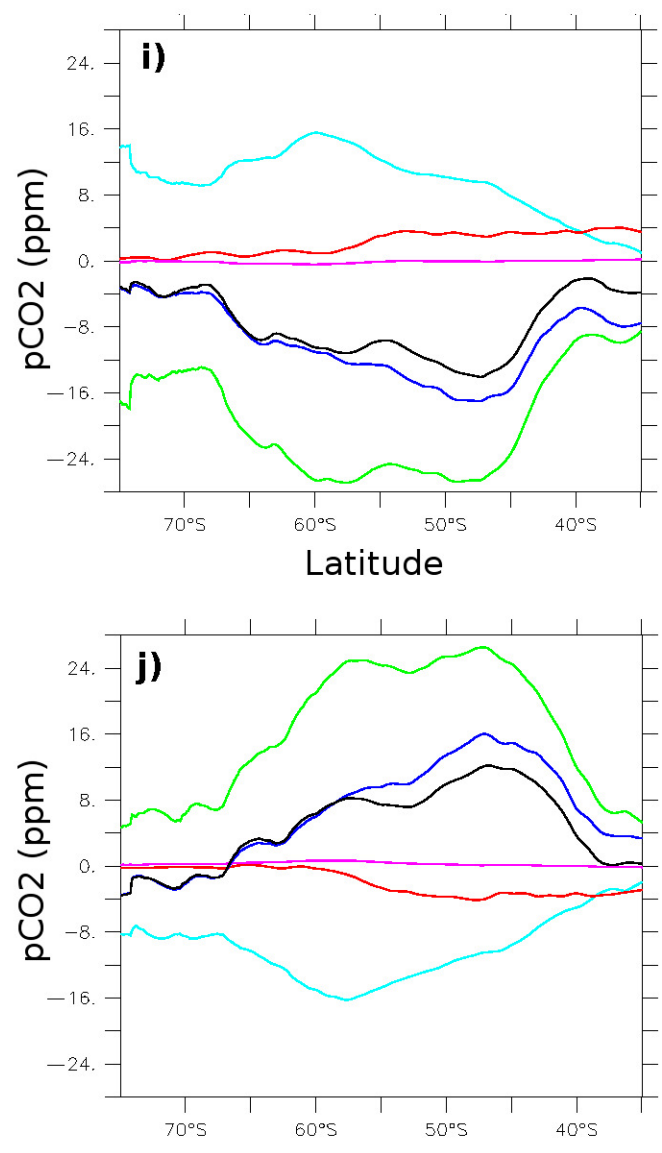

Figure 4.

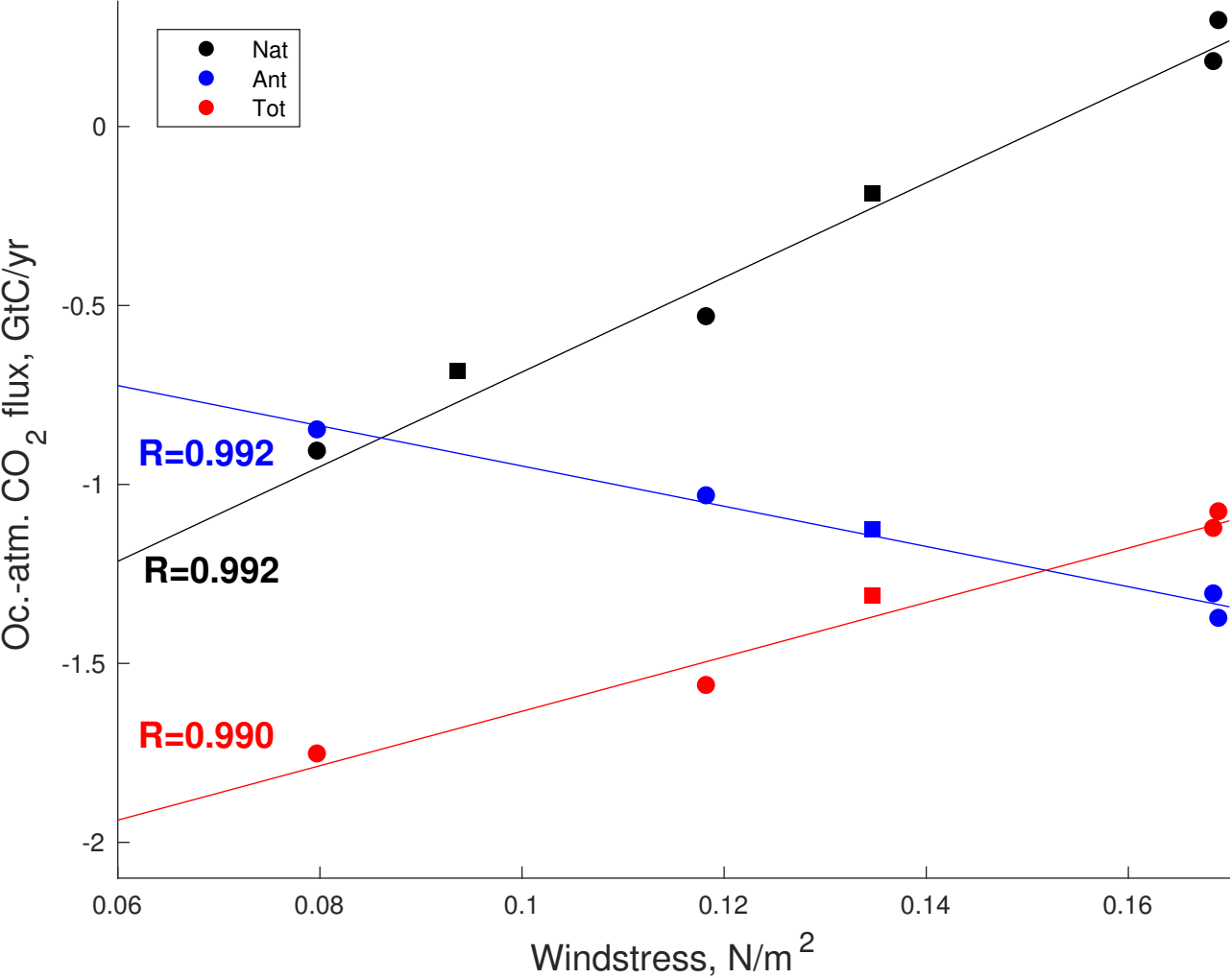
Nat
Ant
Tot
R=0.992
R=0.992
R=0.990
0
-0.5
-1
-1.5
-2
0.06
0.08
0.1
0.12
0.14
0.16
Oc.-atm. CO2 flux, GtC/yr
Windstress, N/m 2

Figure 5.

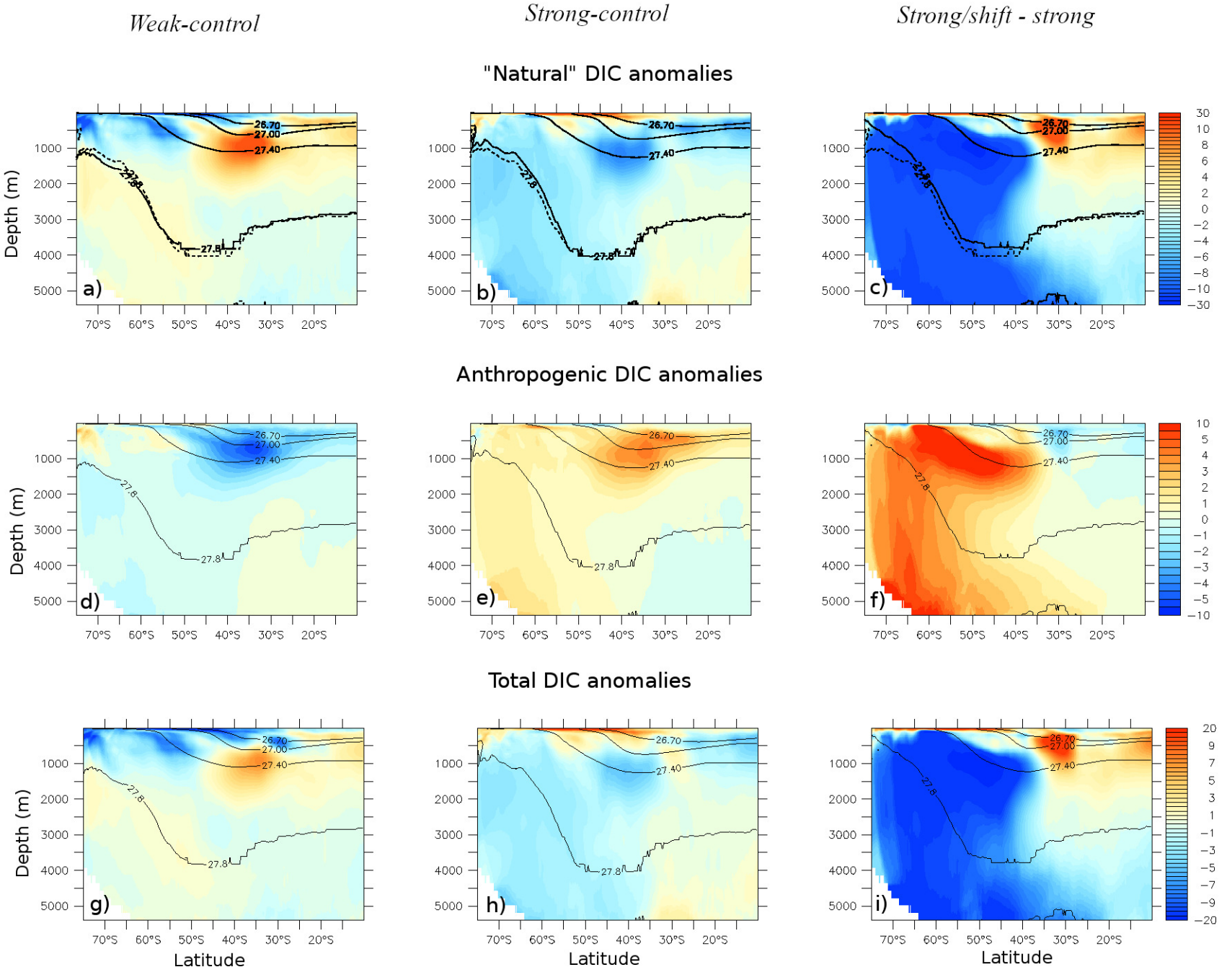
Weak-control
Strong-control
Strong/shift - strong
"Natural" DIC anomalies
Anthropogenic DIC anomalies
Total DIC anomalies
Depth (m)
Latitude
a)
b)
c)
d)
e)
f)
g)
h)
i)
26.70
27.00
27.40
27.8
70°S
60°S
50°S
40°S
30°S
20°S

Figure 6.

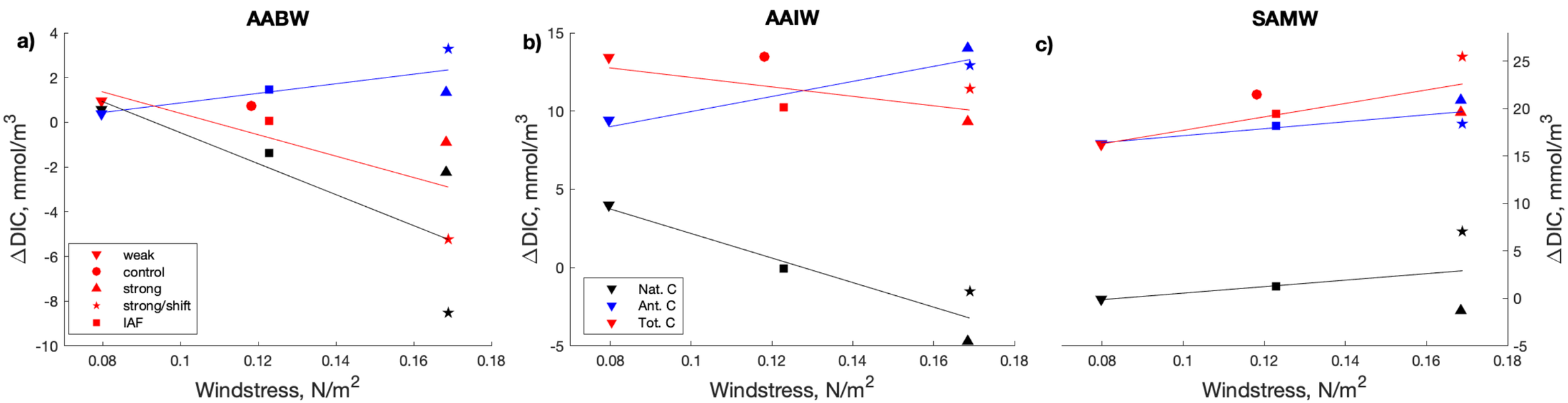
AABW
a)
ΔDIC, mmol/m3
Windstress, N/m2
weak
control
strong
strong/shift
IAF
AAIW
b)
ΔDIC, mmol/m3
Windstress, N/m2
Nat. C
Ant. C
Tot. C
SAMW
c)
ΔDIC, mmol/m3
Windstress, N/m2

Figure 7.

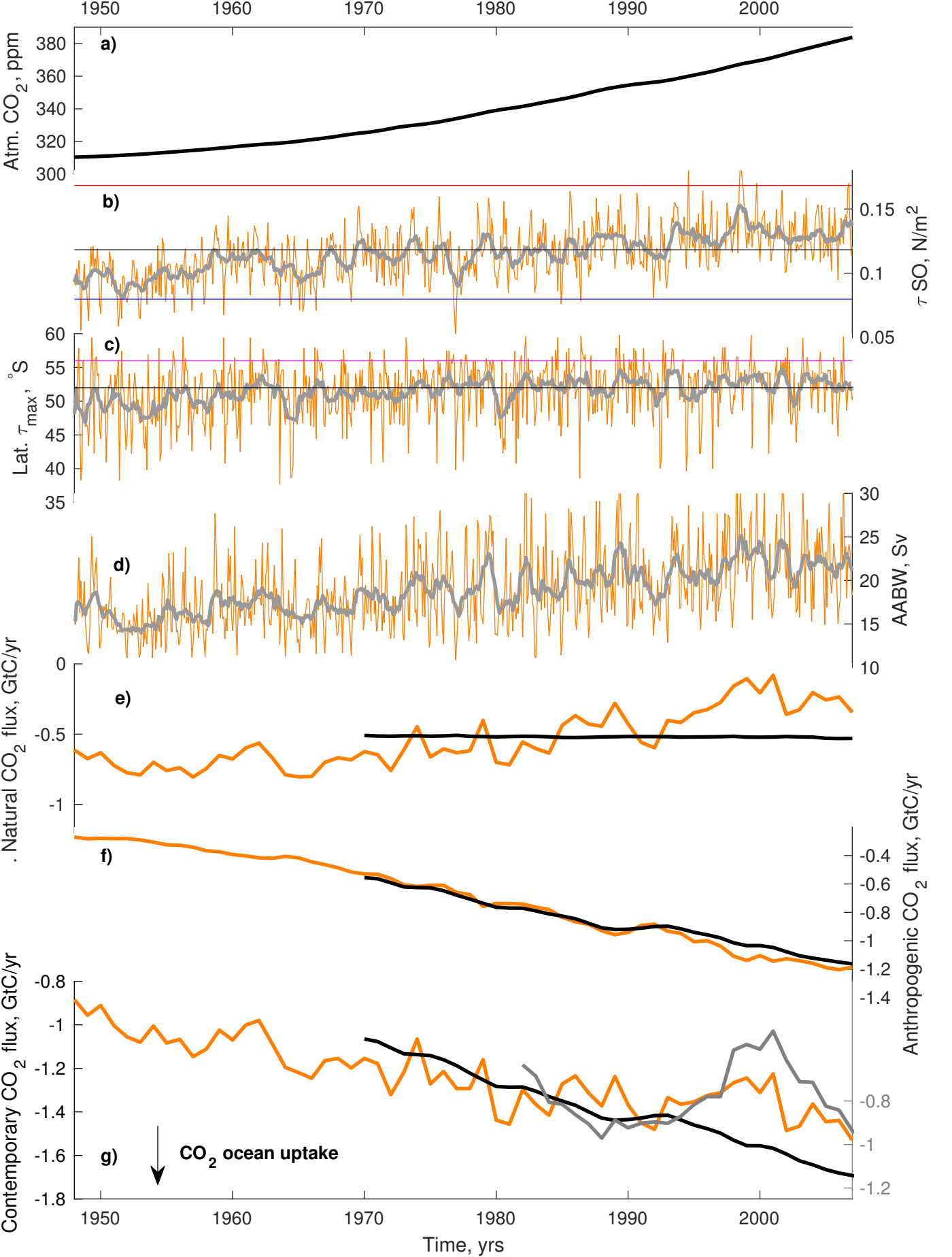
a)
b)
c)
d)
e)
f)
g)
Atm. CO2, ppm
τ SO, N/m2
Lat. τmax, °S
AABW, Sv
. Natural CO2 flux, GtC/yr
Anthropogenic CO2 flux, GtC/yr
Contemporary CO2 flux, GtC/yr
CO2 ocean uptake
Time, yrs

Figure 8.

Contemporary pCO2 trends

1990's

2000's

a)

b)

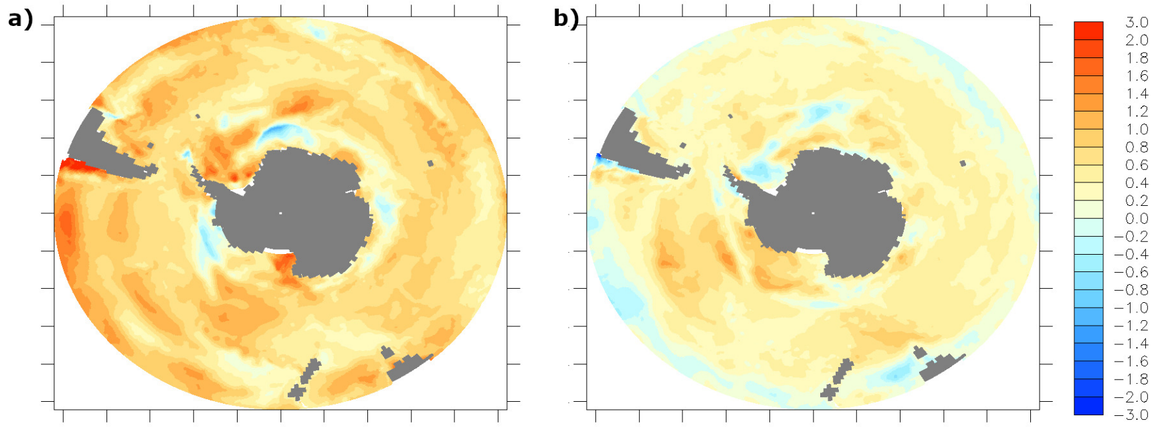

3.0
2.0
1.8
1.6
1.4
1.2
1.0
0.8
0.6
0.4
0.2
0.0
−0.2
−0.4
−0.6
−0.8
−1.0
−1.2
−1.4
−1.6
−1.8
−2.0
−3.0

Contemporary non-thermal trends

c)

d)

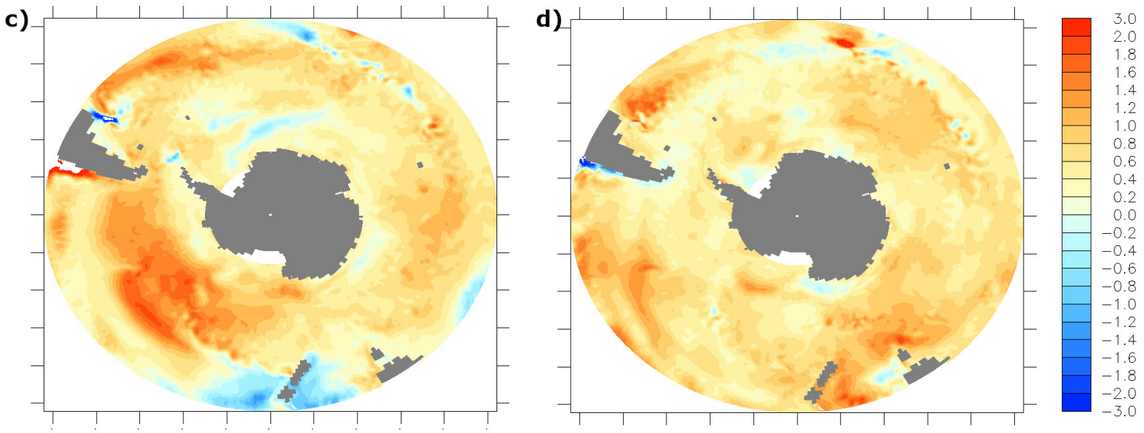

3.0
2.0
1.8
1.6
1.4
1.2
1.0
0.8
0.6
0.4
0.2
0.0
−0.2
−0.4
−0.6
−0.8
−1.0
−1.2
−1.4
−1.6
−1.8
−2.0
−3.0

Contemporary pCO2 trends - SOM-FFN

e)

f)

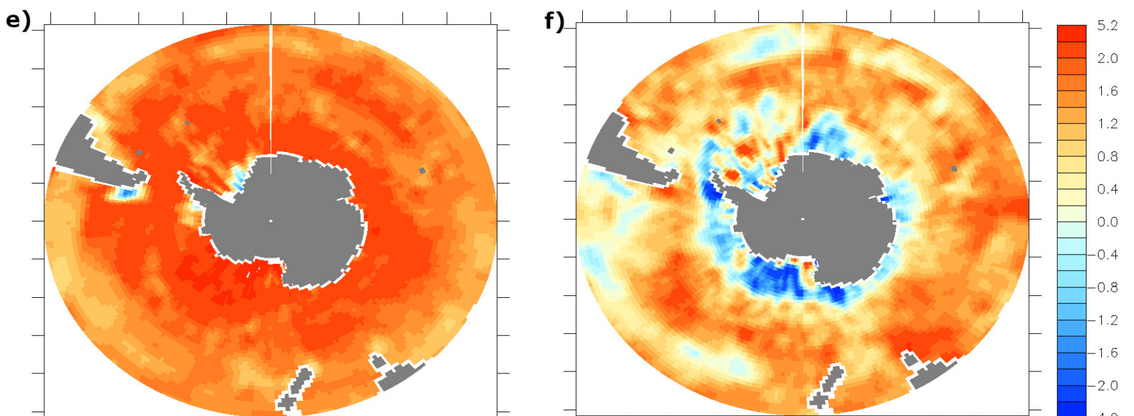

5.2
2.0
1.6
1.2
0.8
0.4
0.0
−0.4
−0.8
−1.2
−1.6
−2.0
−4.0

Natural pCO2 trends

1990's

2000's

g)

h)

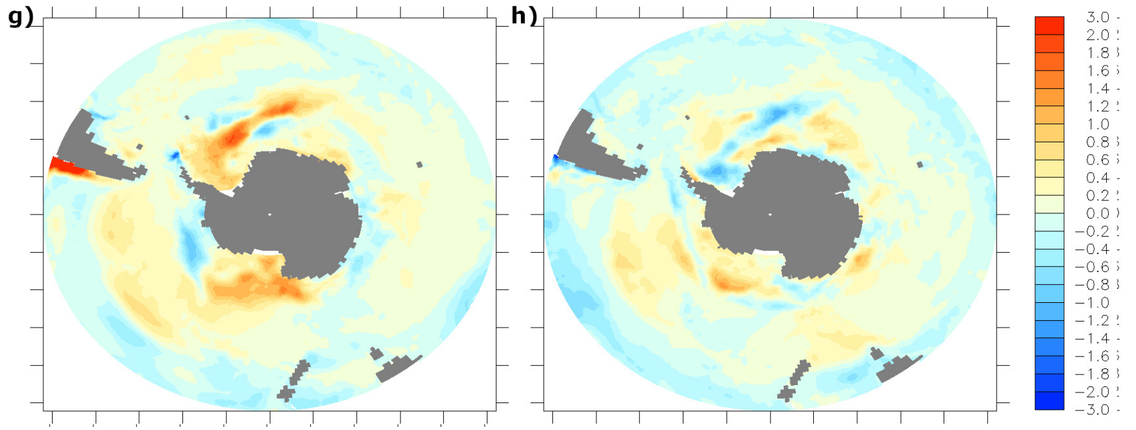

3.0
2.0
1.8
1.6
1.4
1.2
1.0
0.8
0.6
0.4
0.2
0.0
−0.2
−0.4
−0.6
−0.8
−1.0
−1.2
−1.4
−1.6
−1.8
−2.0
−3.0

Natural non-thermal trends

i)

j)

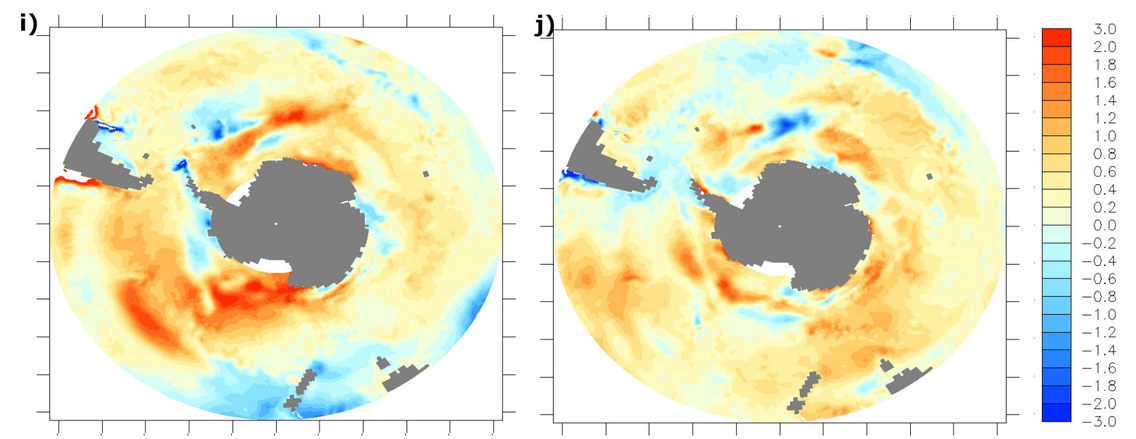

3.0
2.0
1.8
1.6
1.4
1.2
1.0
0.8
0.6
0.4
0.2
0.0
−0.2
−0.4
−0.6
−0.8
−1.0
−1.2
−1.4
−1.6
−1.8
−2.0
−3.0

Thermal trends

k)

l)

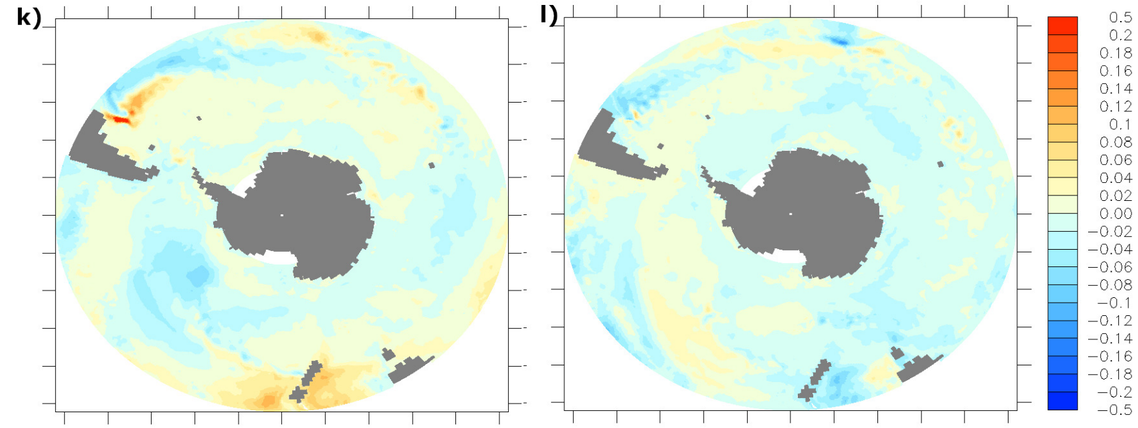

0.5
0.2
0.18
0.16
0.14
0.12
0.1
0.08
0.06
0.04
0.02
0.00
−0.02
−0.04
−0.06
−0.08
−0.1
−0.12
−0.14
−0.16
−0.18
−0.2
−0.5

Figure 9.

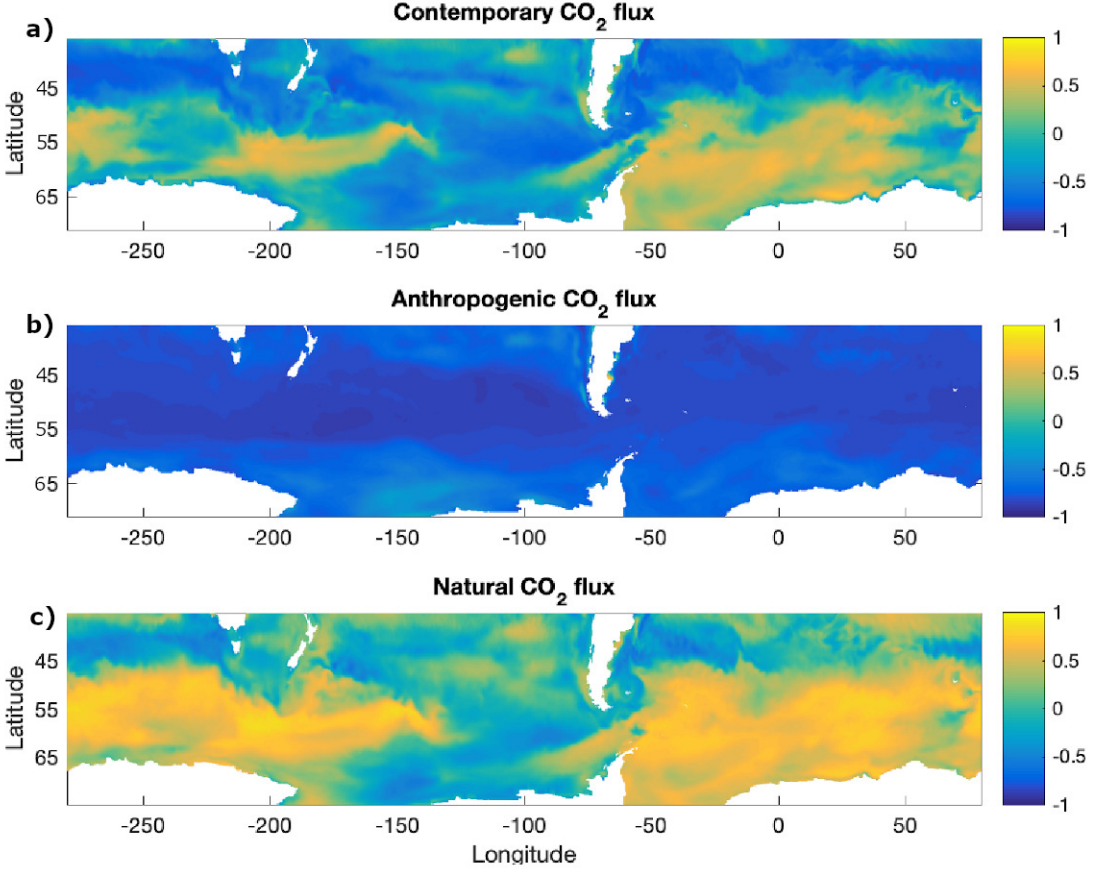
a)
Contemporary CO_2 flux
b)
Anthropogenic CO_2 flux
c)
Natural CO_2 flux
Latitude
45
55
65
-250
-200
-150
-100
-50
0
50
Longitude
1
0.5
0
-0.5
-1

Figure 10.

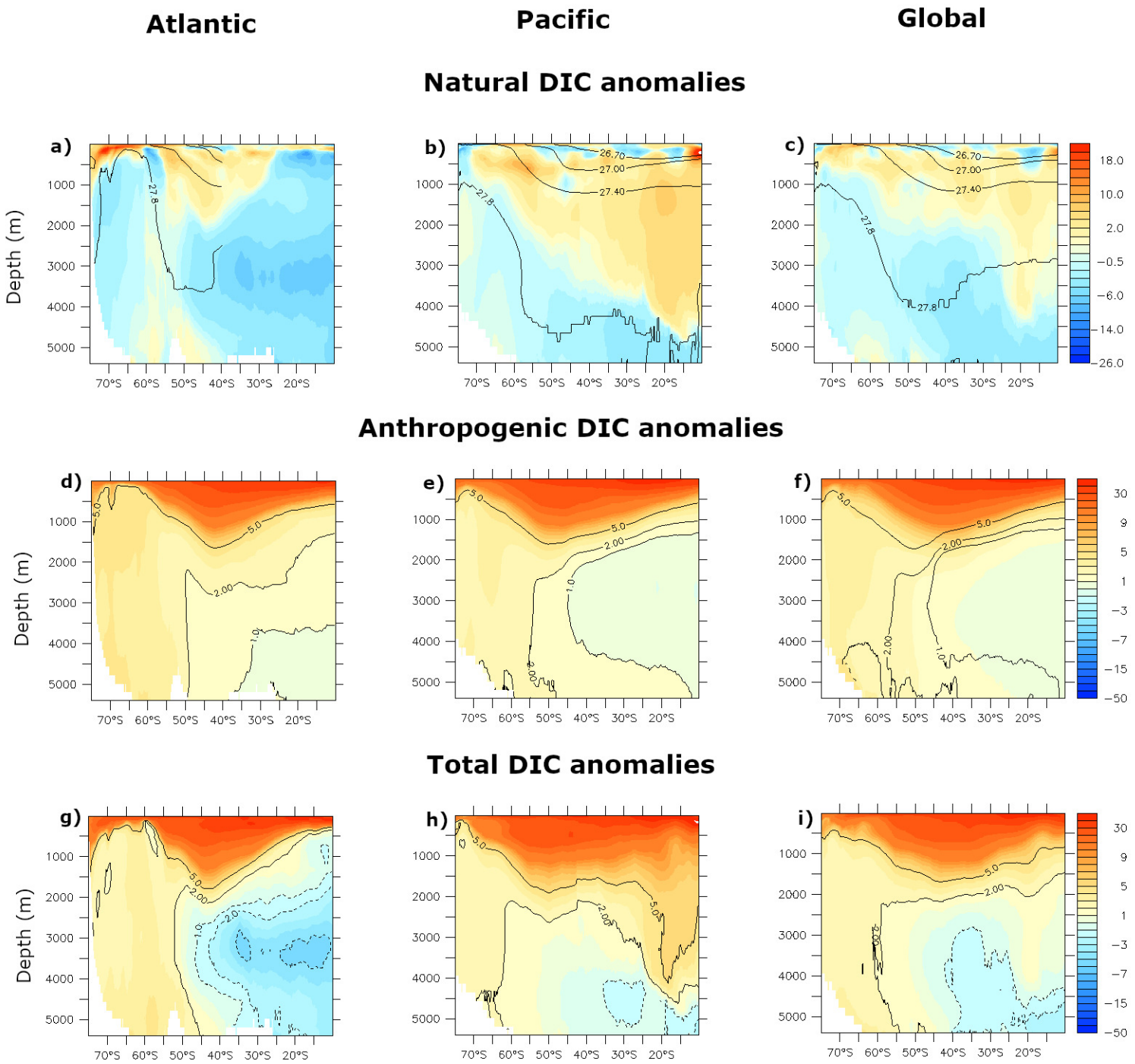
Atlantic
Pacific
Global
Natural DIC anomalies
Anthropogenic DIC anomalies
Total DIC anomalies
a)
b)
c)
d)
e)
f)
g)
h)
i)
Depth (m)
1000
2000
3000
4000
5000
70°S 60°S 50°S 40°S 30°S 20°S
26.70
27.00
27.40
27.8
5.0
2.00
1.0
-2.00
18.0
10.0
2.0
-0.5
-6.0
-14.0
-26.0
30
9
5
1
-3
-7
-15
-50